

Ben-Gurion University of the Negev

**Structural and Refractive Index Profile
Prediction of Fused Optic Fiber Components:
Numerical and Experimental Study**

Thesis submitted in partial fulfilment
of the requirements for the degree of
“DOCTOR OF PHILOSOPHY”

by

Avihai Spizzichino

Submitted to the Senate of Ben-Gurion University
of the Negev

October 2020

Beer-Sheva

Ben-Gurion University of the Negev

**Structural and Refractive Index Profile
Prediction of Fused Optic Fiber Components:
Numerical and Experimental Study**

Thesis submitted in partial fulfilment
of the requirements for the degree of
“DOCTOR OF PHILOSOPHY”

by

Avihai Spizzichino

Submitted to the Senate of Ben-Gurion University
of the Negev

Approved by the advisors

Approved by the Dean of the Kreitman School of Advanced Graduate Studies

October 2020

Beer-Sheva

This work was carried out under the supervision of
Dr. Yuri Feldman and Dr. Sharone Goldring
In the Department of Mechanical Engineering
Engineering Faculty

Handwritten signature of Yuri Feldman in blue ink, written in a cursive style.

Dr. Yuri Feldman

Handwritten signature of Sharone Goldring in blue ink, written in a cursive style.

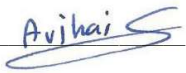
Dr. Sharone Goldring

I Avihai Spizzichino, whose signature appears below, hereby declare that

- I have written this Thesis by myself, except for the help and guidance offered by my Thesis Advisors.
- The scientific materials included in this Thesis are products of my own research, culled from the period during which I was a research student.

Date: 17.10.2020

Student's name: Avihai Spizzichino

Signature: 

This thesis work is dedicated to my parents.

For their endless love, support, and encouragement

עבודה זו מוקדשת להוריי,

על אהבתם הבלתי נגמרת, התמיכה והעידוד התמידי.

Acknowledgements

First, I would like to thank my supervisors, Dr. Yuri Feldman and Dr. Sharone Goldring, for their guidance and support throughout the study. Thank you for your confidence in me. Without you, it would not have happened.

I would like to thank my wife - thank you for your understanding and encouragement in many critical moments along the road. Thank you for all your sacrifices, which allowed me to implement this study and for your friendship, which makes my life beautiful. Thank you - you are a great part of my life.

I would also like to thank my family: my wonderful children, my parents, my brother and sisters, and my lovely dear grandmother Julia Fornaro Spizzichino, for being a significant part of my personality and for all the support and confidence in my success during my whole life.

Finally, I would like to thank my friends - thank you for your support, advice and long periods of a good time. I cannot list all the names here, but you are all always in my mind.

This endpoint of the study is just the beginning of other new things,

Thank you all.

Abstract

Couplers and other fused fiber optic components are integrated in many optical systems. Such devices make it possible to couple light between two fibers (2x2 coupler) or combine or split light between several fibers and one central fiber (Nx1 combiner). Common to all such devices is that they are fabricated by heating, pulling, and fusing tightly packed optical fibers. The optical behavior of a coupler or combiner depends on its external shape and on the refractive index profile, which is dictated by internal dopants and their concentration-distribution. Over the years, many models and simulation tools have been developed to predict the optical behavior of such components, provided that their shape and index of refraction are well defined. Previous research enabled the prediction of the structure of some fused fiber components. However, theoretical tools that can predict the external shape and the refractive index profile are still not accurate or general enough to facilitate accurate optical simulations. Lacking such a tool, the development of new fused fiber components requires many iterations of trial and error, which makes the process long and expensive.

The main purpose of this study is to obtain a generic solution based on numerical simulations to predict the structural evolution of the fiber components containing a number of fibers in any configuration. The numerical tool should also include the solution of a convection-diffusion equation in order to predict the evolution of dopant concentration. Additionally, it was aimed that the solver will be generic so as to be able to address two-phase flow problems in other physical areas.

The study consisted of two main phases: a. developing the appropriate numerical foundations and tools, and b. experimental study and analysis of the dynamic evolution of fused fiber optic components during fabrication. The

experimental results were then compared to the numerical prediction and provided a realistic test case for further study.

First, we developed the numerical methodology based on the Immersed Boundary (IB) and Front Tracking methods. The methodology makes it possible to couple the continuity and momentum equations for incompressible two-phase flow with the solution, where the pressure and surface tension forces serve as Lagrange multipliers. One of the advantages of this approach is the implicit fulfillment of mass conservation (with or without source) and the prevention of mass leakage.

The numerical methodology was implemented in a numerical solver and extensively validated by comparing the simulation results with previously published data for four benchmark test cases. Each benchmark case was distinguished by the driving force, starting from a rising bubble, followed by a drop under shear flow, and, lastly, rosette relaxation. We also simulated problems that include body-splitting due to a high-density ratio between the fluids and a high-velocity gradient. The comparison for all the test cases indicated an accurate solution of the problems.

After laying the numerical foundations, the study proceeded to the experimental phase. Fused optic fiber components were fabricated and characterized; the results were then compared to the corresponding numerical results. Four different configurations were experimentally tackled. In the first, the most basic type of coupler was fabricated from two identical fibers, in order to examine the fully symmetric configuration. The second type was referred to as the pump-SMF coupler and was also fabricated from two fibers differing only internally– the external interface of the coupler was thus regarded as being symmetric, while the core-refractive index of the fibers was not. The third type of coupler constituted a fully non-symmetric configuration, i.e., fusion of two

fibers that were different both externally and internally. The fourth configuration has the most complex geometry - that of non-circular fiber tapering. For all the configurations, good agreement was obtained by qualitatively and quantitatively comparing the numerical simulation and the experimental results. In all cases, the velocity field was obtained by the solution of continuity and NS equations, and the dopant concentration evolution by solving the convection-diffusion equation. Additionally, the fibers' viscosity was functionally reduced in accordance with the OH absorption.

Besides the numerical and experimental comparison, we also simulated several configurations of non-symmetric couplers characterized by various aspect ratio values in order to identify the relations between the aspect ratio and the fusion of the couplers.

The developed numerical tool can also successfully handle the time evolution of much more complex multi-fiber configurations, incorporating many contact points for each fiber and also including the non-negligible amount of air trapped between the boundaries of adjacent fibers. A representative example of such a simulation is also presented.

Table of Contents

| | |
|--|----|
| List of Figures..... | I |
| List of Symbols..... | IV |
| Chapter 1: Introduction..... | 1 |
| Chapter 2: Theoretical background | 9 |
| 2.1 Governing equations..... | 10 |
| 2.1.1 Discretization in time and space..... | 13 |
| 2.2 Numerical methods | 15 |
| 2.2.1 Immersed Boundary method..... | 15 |
| 2.2.2 The numerical methodology..... | 16 |
| Chapter 3: Validation study | 20 |
| 3.1 Test case 1 - Rising bubble without break-up..... | 21 |
| 3.2 Test case 2 - Rising bubble undergoing break-up | 26 |
| 3.3 Test case 3 - Drop under shear flow..... | 30 |
| 3.4 Test case 4 - Rosette shape..... | 33 |
| 3.5 Additional capabilities of the algorithm..... | 36 |
| 3.6 Test case 5 – Fiber optic coupler | 40 |
| Chapter 4: Experimental setup..... | 43 |
| Chapter 5: Calibration and similarity analysis | 46 |
| Chapter 6: Results | 49 |
| 6.1. The numerical simulations and the experimental results | 50 |
| 6.1.1. Symmetric two-SMF coupler | 50 |
| 6.1.2. Pump-SMF coupler..... | 53 |
| 6.1.3. Non-Symmetric coupler | 55 |
| 6.1.4. Fiber with a non-circular cross section | 57 |
| 6.2. Characterization of the non-symmetric couplers..... | 60 |
| 6.3. Advanced modeling of multi-fiber combiners | 61 |
| Chapter 7: Summary and conclusions..... | 63 |
| 8. References | 65 |
| Appendix I..... | 72 |
| Appendix II..... | 74 |

List of Figures

| Number | Description | page |
|--------|--|------|
| 1.1 | Model of fusion. The tangent arcs are calculated so that the hatched area is equal to the cross-hatched area [8]. | 2 |
| 1.2 | Cross-section of a 2×2 coupler for degrees of fusion ranging from 0 to 1 [8]. | 2 |
| 2.1 | Schematic diagram of the fibers' coupling process. | 9 |
| 2.2 | Schematic representation of a two-phase flow configuration. | 11 |
| 2.3 | Control volume for pressure field – staggered grid arrangement. | 15 |
| 2.4 | Block diagram of the computational time step. | 19 |
| 3.1 | Initial configuration and boundary conditions of rising bubble test flow. | 22 |
| 3.2 | Bubble shapes obtained on four different grids at time $t = 3$. | 23 |
| 3.3 | Bubble shapes obtained at final time ($t = 3$): comparison between the present and the previously published results. | 24 |
| 3.4 | Time evolution of the circularity values. | 24 |
| 3.5 | Time evolution of the Y position of the center of mass. | 25 |
| 3.6 | Time evolution of the rise velocity. | 25 |
| 3.7 | Schematic bubble break-up modeling. | 27 |
| 3.8 | Time evolution of the rising initially cylindrical bubble obtained on a 320×640 grid for the value of $\alpha = 1.5$ and zero initial velocity. | 29 |
| 3.9 | Initial state of the circular drop submerged into a fully developed Couette flow. | 30 |
| 3.10 | Drop shapes at $t=3$: (a) $Ca=0.2$, $\mu_r = 1$; (b) $Ca=0.2$, $\mu_r = 10$; (c) $Ca=0.4$, $\mu_r = 1$; and (d) $Ca=0.4$, $\mu_r = 10$. | 32 |
| 3.11 | Initial configurations of rosette-shaped drop corresponding to $n=3, 5$, and 8 modes. | 33 |
| 3.12 | Verification of the time instances of a rosette drop characterized by $3, 5$, and 8 modes initial shape when relaxing to circular disc in quiescent liquid. | 35 |
| 3.13 | The magnitude of parasitic velocities observed for a drop of circular disc shape. | 36 |
| 3.14 | Interface evolution of circular drop under pure shear flow undergoing multiple break-up phenomena, $Re=1$, $We=7.2$, 10×1 channel. | 38 |
| 3.15 | Interface evolution of circular air bubble rising in water. The simulations were obtained for $Re=300$, $We=2.6$, and $Fr=1$. | 40 |

| | | |
|------|--|----|
| 3.16 | Initial configuration of two SMF28 fibers: A, B, and C represent air, the fused silica fibers, and the concentration of dopants, respectively. | 41 |
| 3.17 | Comparison of the simulation results (solid red line) obtained in the current work (<i>left</i>) to the results of Pone et al. [1] (<i>right</i>). The cross-sections are at: (a) $f = 0.355$, (b) $f = 0.6$, and (c) $f = 0.92$. | 42 |
| 4.1 | Illustration of the glass processing workstation. | 43 |
| 4.2 | The measurement setup. | 44 |
| 4.3 | Initial configurations of the analyzed cases: fully symmetric case, symmetry only of the external interface, non-symmetric case, and complex geometry. | 45 |
| 5.1 | Time evolution of the degree of fusion for several values of the viscosity. ($vs = 0$). | 46 |
| 5.2 | Geometric dimensions of a typical coupler. | 47 |
| 5.3 | Evolution of the degree of fusion for several viscosity values as a function of the aspect ratio of the coupler ($vs=0$). | 48 |
| 6.1 | Experimentally and numerically obtained cross-sections of a fully symmetric SMF fiber coupler at different time instances: 30 s, 1650 s, 3600 s, and 5300 s. | 52 |
| 6.2 | Comparison between the numerically and experimentally obtained temporal evolutions of the cross-sectional area and the MFD typical of the symmetric coupler. | 52 |
| 6.3 | Comparison between the numerically and the experimentally obtained temporal evolutions of the MFD as a function of the coupler dimensions typical of the symmetric coupler. | 53 |
| 6.4 | Experimentally and numerically obtained cross-sections of pump (125/106 μ m) and SMF (125/8 μ m) fiber coupler at different time instances: 210 s, 2100 s, 4400 s, and 7500 s. | 54 |
| 6.5 | Comparison between the numerically and the experimentally obtained temporal evolutions of the cross-sectional area and the MFD typical of the second test case. | 55 |
| 6.6 | Comparison between the numerically and experimentally obtained temporal evolutions of the MFD as a function of the coupler dimensions for the second test case. | 55 |
| 6.7 | Experimentally and numerically obtained cross-sections of non-symmetric coupler at different time instances: 30 s, 1350 s, 4300 s, and 7000 s. | 56 |
| 6.8 | Comparison between the numerically and the experimentally obtained temporal evolutions of the cross-sectional area and the MFD typical of the non-symmetric coupler. | 57 |
| 6.9 | Comparison between the numerically and the experimentally obtained temporal evolutions of the MFD as a function of the coupler dimensions for the non-symmetric coupler. | 57 |

| | | |
|------|--|----|
| 6.10 | Experimentally and numerically obtained cross-sections of the non-circular tapered fiber coupler at different time instances: 10 s, 1320 s, 2500 s, and 5000 s. | 58 |
| 6.11 | Comparison between the numerically and the experimentally obtained temporal evolutions of the cross-sectional area and the MFD typical of fiber with a non-circular cross section during tapering. | 59 |
| 6.12 | Comparison between the numerically and the experimentally obtained temporal evolutions of the MFD as a function of the coupler dimensions for fiber with a non-circular cross section. | 59 |
| 6.13 | Simulated 3D structure of: a symmetric coupler, a coupler composed of pump (125/106 μ m), and SMF (125/8 μ m) fibers, a non-symmetric coupler, and a tapered non-circular fiber. | 60 |
| 6.14 | Simulation results of the MFD related to the height-width (H/W) ratio of the coupler for several initial ratios. | 61 |
| 6.15 | Simulation results for a combiner composed of 7 fibers at the initial state, 900 s, 2500 s, and 5000 s. | 62 |

List of Symbols

| Roman Letters | Description |
|---------------|--|
| A_0 | Initial cross-sectional area of the fibers forming the coupler |
| $A(t)$ | Cross-sectional area taking place at time t |
| C | Courant number criterion |
| c | Dopant concentration |
| \tilde{D} | Diffusion coefficient |
| D | Characteristic length scale (usually diameter) |
| d | Fiber center separation |
| $d(r)$ | Dirac delta functions |
| \bar{e}_y | Unit vector in the Y direction |
| \mathbf{f} | Surface tension force density |
| \tilde{f} | The degree of fusion (by Lacroix et al., Eq (1.1)) |
| f | The degree of fusion |
| f_m | Modified fusion degree (MFD) |
| g | Gravitational acceleration |
| H | Helmholtz operator |
| H / W | Coupler aspect ratio |
| h | Number of grid cells in the shortest direction |
| \mathbf{I} | Identity matrix |
| I | Indicator function |
| IC | Interface Curvature operator |
| L | Total length of immersed boundary interface |
| l | Flame scanning length |
| \mathbf{n} | Interface normal |
| n | Time step-index |
| p | Pressure |
| q | Volumetric sink |

| | |
|--------------|---|
| r_d | Radius of cladding |
| r_{12} | The initial radii of the fibers |
| Δr | Cell width in the r direction |
| t | Time |
| \mathbf{u} | Velocity field |
| u | Velocity in x direction |
| v | Velocity in y direction |
| v_s | Fibers pulling rate |
| W_0 | The initial width of the coupler |
| W_∞ | The theoretical final width of the coupler |
| \mathbf{X} | Coordinates of the immersed boundary |
| \mathbf{x} | Local coordinates |
| Ca | Capillary number, $Ca = We / Re = U\mu_{\min} / \sigma$ |
| Fr | Froude number, $Fr = U(gD)^{-1/2}$ |
| Re | Reynolds number, $Re = \rho_{\min} UD / \mu_{\min}$ |
| We | Weber number, $We = \rho_{\min} U^2 D / \sigma$ |

Greek Letters

| | |
|-----------|------------------------------|
| δ | Distribution function |
| λ | OH absorption rate |
| μ | Dynamic viscosity |
| μ_0 | Initial viscosity |
| μ_s | Viscosity at saturated state |
| ρ | Fluid density |
| σ | Surface tension coefficient |
| ψ | General variable |

| | |
|----------|--------------------------------|
| Γ | Interface of the immersed body |
| ϕ | Degree of circularity |
| Ω | Computational domain |

Chapter 1: Introduction

Fiber optic components have diverse structures and applications, ranging from simple 2×2 symmetric couplers, through fiber-laser pumps and signal combiners, to even more complex systems such as photonic lanterns [2, 3]. Many of these fiber optic components are fabricated by the so-called “heat-and-pull” technique, in which optical fibers are fused and tapered simultaneously. The popularity of the technique may be attributed to the simplicity of the setup and the ability to fabricate a wide range of optical components that accurately meet a variety of design requirements. The “heat-and-pull” technique includes three fundamental steps: gathering and arranging the optical fibers in a particular initial order, subjecting the fibers to viscous flow sintering, and subsequently pulling the fibers. This production process affects both the external geometry of the produced fiber optic component and the distribution of the internal dopant concentration. The functionality of fused fiber optic components thus depends on their structure and the concentration profile of the inner dopants.

A number of models and simulation tools predicting the optical functionality and the light transmission characteristics of particular fiber components have been developed over the years and are well established today [4, 5, 6]. However, all the developed tools require the precise geometry of the given fiber component as input. Without this information, the result of any modeling tool will not be sufficiently accurate. This drawback becomes particularly critical for complex combiners whose light transmission characteristics are especially sensitive to the geometry of the component and the concentration profile of the internal dopants. Therefore, the development of complex fiber components typically requires conducting a series of preliminary

on-site experiments, which can significantly lengthen R&D times and increase production costs.

We now briefly review some of the main studies that have focused on modeling the structure of fiber optic components. Lacroix et al. [7] empirically approximated the cross-sectional shape of two identical fused fibers by imposing the principle of conservation of matter. In this model, the fused fibers are assumed to overlap each other. The overlapping area of the cladding is transferred to the sides of the fibers by assuming that a circular arc limits the coupler cross-section (see Fig. 1.1).

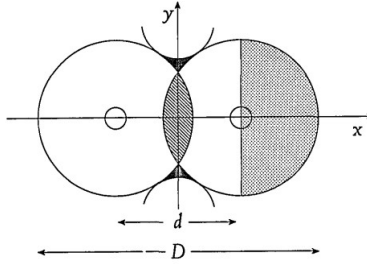


FIG. 1.1 Model of fusion. The tangent arcs are calculated so that the hatched area is equal to the cross-hatched area. D is the width of the coupler cross-section, d is the fiber center separation [7].

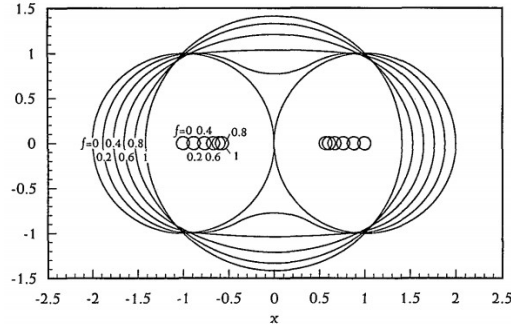


FIG. 1.2 Cross-section of a 2×2 coupler for degrees of fusion ranging from 0 to 1. [7]

This model makes it possible to predict the cross-sectional shape as a function of the degree of fusion (0 for tangent fibers and 1 for full fusion – circular cross-section), as shown in Fig. 1.2. The degree of fusion is defined by

$$\tilde{f}_{2 \times 2} = \frac{2r_{cl} - d}{2(2 - \sqrt{2})r_{cl}}, \quad (1.1)$$

where r_{cl} is the cladding radius of the unfused fiber and d is the fiber center separation. The model has demonstrated good agreement with experimental results. However, it lacks any physical coupling with the evolution-dynamics of the couplers' shape and predicts only the final outer boundary of cladding and the center of mass of the core. This approach is limited and does not allow for addressing other critical phenomena, such as deformation of the optical component and diffusion of the dopants within the component core, or for predicting the fusion characteristics of the optical components produced from initially more complicated structures.

Other research groups have tackled the problem by developing models based on solving the Navier-Stokes (NS) equations. The studies of Garabedian [8] and Richardson [9, 10], for example, analyzed the dynamic plane Stokes-flow of a viscous incompressible fluid bounded by a smooth closed curve driven solely by the surface tension force. Their analysis was based on conformal mapping and predicted the shape evolution as a function of the fusion rate. Hopper [11, 12, 13] developed an advanced model predicting the temporal evolution of the component's shape by using conformal mapping in the complex z plane. However, this method required the assumption of a parametric form based on approximated shape functions, and it thus cannot be applied to optic fiber components of arbitrary initial geometry. In 1997, Richardson [14] revisited and extended his and Hopper's models by addressing the configuration of a circular cylinders unclosed array. He established this model by two-dimensional (2D) simulations of touching circular discs developing into one symmetric circle and showed that when there are N discs in a general position, the evolution of the fluid region can be described by a conformal map involving $2N-1$ time-dependent parameters governed by N invariants and $N-1$ first-order differential equations. In his next study, Richardson [15] considered the corresponding problems when the fluid occupies a double-connected region, which is equivalent to a bundle of fused

fibers. In both models, only the flow at the surface of the coupler was treated. To this point, a generalized solution allowing for prediction of the internal parameters, rather than only the outer surface behavior, was missing.

Of particular interest are the studies of Pone et al. [1, 16], who investigated the refractive index profile of fused optic fiber coupler cross-sections. They presented numerical simulations that were based on the solution of continuity and NS equations as well as a convection-diffusion equation, and compared the numerical results to experiments that fundamentally studied the fusion of two SMF28 fibers, $125\mu m$ in diameter. The fibers were brought into contact and heated by a propane micro-torch at a temperature of about $1400^\circ C$, and then the degree of fusion and the external shape of the fused fibers were characterized. The degree of fusion without pulling as defined in [1] is given by

$$f(v_{pull} = 0) = \frac{W_0 - W(t)}{W_0 - W_\infty}, \quad (1.2)$$

where W_0 , W_∞ are the initial and the theoretical final widths of the coupler: $W_0 = 2r_1 + 2r_2$, $W_\infty = 2\sqrt{r_1^2 + r_2^2}$. r_1 and r_2 are the initial radii of the fibers. In contrast to other studies, they also considered the diffusion of the core governing the evolution of the dopants' concentration inside the fibers.

Despite progress in simulations of fiber optic components and the excellent agreement between the numerical and experimental measurements presented by Pone et al. [1], a generic tool to simulate the structure and the refractive index distribution of complex fused fiber components is not readily available. The need for the development of a high-fidelity structural simulation tool for facilitating the fabrication of components is particularly evident for complex systems whose fabrication is challenging due to their high optical sensitivity to tiny structural variations.

The current study focuses on the development of a theoretical framework based on the numerical solution of quasi-three-dimensional (3D) incompressible NS equations formulated for immiscible two-phase flow. Modeling of fiber optic components requires understanding of optical fibers and fabrication processes, combined with knowledge of numerical methods for simulation of two- and multi-phase flow. In practice, numerical modeling of multiphase flows is a broad topic which plays a significant role in the solution of many applied science and engineering problems in the fields of environmental and geophysical science [17, 18], biomechanical engineering [19, 20], chemical processing [21] and the fabrication of optical waveguides. The simulation of two-phase flows is challenging since it includes modeling of interactions between the different phases, tracking the boundary interface, and in some cases, resolving solidification and melting phase changes. Several numerical techniques have been developed for modeling two-phase flows with deformable interfaces and free boundaries. Typically, the techniques are classified in terms of the multi-physics phenomena modeled: the flow modeling, the interface modeling, and the coupling between the two [22].

There are two basic numerical approaches that deal with free-interface two-phase flow: interface-tracking and interface-capturing. In the interface-tracking approach, the interface is determined by a series of Lagrangian markers, whose location is dynamically updated throughout the numerical simulation. Front Tracking (FT) [23, 24] and Immersed Boundary (IB) [25, 26, 27, 28] methods are typical examples of the interface-tracking approach. In the interface-capturing approach, the interface is reconstructed from a Eulerian scalar field characterizing the flow properties. This approach includes the Volume Of Fluid (VOF) [24, 29], Level Set (LS) [24, 30], and Phase-Field (PF) methods [24, 31, 32].

The present study focuses on the development of a formulation based on the interface-tracking approach and the direct forcing IB method [33, 34] to

resolve the two-phase interface. The IB method was initially introduced by Peskin [25, 26] for simulation of blood dynamics in the cardiac chambers. The method is suitable for the simulation of flows in the presence of a number of immersed bodies of arbitrary geometry. Each body is determined by a set of Lagrangian points, which do not necessarily coincide with the underlying Eulerian grid. In the most general case, the body can be deformable and moving. In the direct forcing IB approach, the kinematic non-slip constraints at all the points of the body are enforced by applying Lagrangian forces entering as sources into the NS equations. The values of the applied forces are unknown a priori and are a part of the overall solution of the problem. In single-phase flows, the values of the Lagrangian forces are coupled with the pressure and velocity fields governed by the NS equations. In immiscible two-phase flows, the simulation should also account for the surface tension forces coupling the fluid characteristics of each phase with the unknown dynamically evolving curvature of the interphase interface.

The accuracy of any two-phase numerical simulation employing the interface-tracking approach depends on a precise evaluation of the Lagrangian forces on the interface between the two phases. The forces comprise the kinematic constraints for continuous values of shear stress and velocity vectors. Historically, numerical simulations relied on explicit treatment of Lagrangian forces (see e.g., Li et al. [28], Rutka, and Li [35]). The surface tension forces are explicitly calculated based on the interface curvature obtained at the previous time step, while the NS equations are solved by the SIMPLE [36] algorithm. The above methodology can be easily plugged into any existing time marching solver of the NS equations based on a segregated pressure-velocity coupling, which explains its high popularity for simulation of both single- and two-phase flows [33, 34, 37, 38]. However, the explicit scheme has a number of disadvantages. First, the kinematic constraints are applied to the intermediate velocity field, which has to be further projected to a divergence-free subspace. As a result, a non-negligible mass leakage through the interface between the two phases typically shows up after completing the correction-projection step. To improve the accuracy and to ensure the mass conservation of the explicit direct forcing IB formulation, a number of techniques

have been proposed. Worthy of note are the works of Kempe et al. [39, 40], who imposed substantially more accurate boundary conditions on the IB surface by introducing intermediate iterations. An additional important study was published by Li et al. [41], who proposed an area preservation correction scheme by correcting the interface location normally to the interface so that the area remains constant. More recently, Bao et al. [42] proposed improving volume conservation by applying a continuous velocity interpolation operator that is divergence-free and a new force-smearing operator that joins with the interpolation operator and ensures the energy conservation.

In the numerical part of the present study, we focus on a fully coupled approach in which the momentum and the continuity equations and the Lagrangian forces, expressed as the distributed Lagrange multipliers, are fully coupled. The developed fully coupled approach offers an attractive alternative to the explicit coupling approach. The idea was originally proposed by Glowinski et al. [43], who introduced the Distributed Lagrange Multiplier method (DLM) for simulations of 2D flow around a moving disc [43]. An extension of this study was conducted in simulations of particulate flows [44, 45, 46] and a fluid/flexible-body interaction [47]. An additional contribution to the development of the fully coupled DLM approach was due to the work of Taira and Colonius [48], who implemented it within the framework of a projection method. The latest theoretical development of the coupled DLM approach is owing to Feldman and Gulberg [49], who extended the fully coupled approach to the linear stability analysis of pressure and thermally-driven 2D flows. The idea underlying all the implementations of the fully coupled DLM approach is that the initial system of equations is extended by including additional relationships implicitly linking the Euler flow fields and the distributed Lagrange multipliers, enforcing kinematic constraints imposed by the surfaces of immersed bodies. The main purpose of the present study is to develop and to verify extensively a novel IB formulation employing the fully coupled DLM approach for simulating two-phase immiscible flows. The developed methodology belongs to the family of FT methods and provides precise conservation of mass of both phases without the need for any

additional correction procedure. In the present formulation, the surface tension forces, which are proportional to the curvature of the interphase interface, are introduced as distributed Lagrange multipliers, and play the role of kinematic constraints providing impermeability of both phases. The Fully Pressure-velocity Coupled Direct solver (FPCD), originally developed by Feldman and Gelfgat [50] for the simulation of shear- and thermally-driven confined flows, is used as a “driver” for presenting the capabilities of the developed methodology. The principle novelty of the developed approach stemming from the implemented fully coupled DLM formulation is twofold. First, the kinematic constraints providing impermeability of both phases are accurately met. Second, the developed approach provides accurate volume conservation of both phases without the need for additional correction procedures.

An additional part of this study is the fabrication of optic fiber components that would serve as experimental validation for the developed numerical model. The experiments are based on a destructive method and include ‘slice and polish’ to track the outer interface of simple and complex cross-sections of fiber components, and evaluate the dopants' concentration distribution.

The rest of the thesis is organized as follows. The second chapter presents a theoretical background, including the governing equations of the impermeable two-phase flow and implementation details of the IB and FT techniques. The third chapter comprises a verification study focused on simulations of three representative two-phase benchmark flows. The fourth and fifth chapters present the experimental production and diagnostic set up, followed by comparing the numerical and experimental results and extensive discussions. The major conclusions, as well as suggestions for future work, are then presented in the last chapter.

Chapter 2: Theoretical background

The fabrication of fiber couplers by the "heat-and-pull" technique requires a heat source (a hydrogen flame in our case) and stages to hold and pull the fibers. The tapering rate is determined by the pulling speed and the temperature distribution of the heated zone. The temperature distribution during the process is, in turn, controlled by the flame intensity, the flame-to-fiber distance, and the flame scanning rate and length. To obtain an effective isothermal heating zone, the flame scanning rate must be much higher than the rate of fiber pulling. Providing that the above conditions are maintained, the active heating zone is equivalent to the flame scanning length. In summary, the flame scanning length determines the heating zone, and the stage pulling speed controls the tapering rate (see Fig. 2.1).

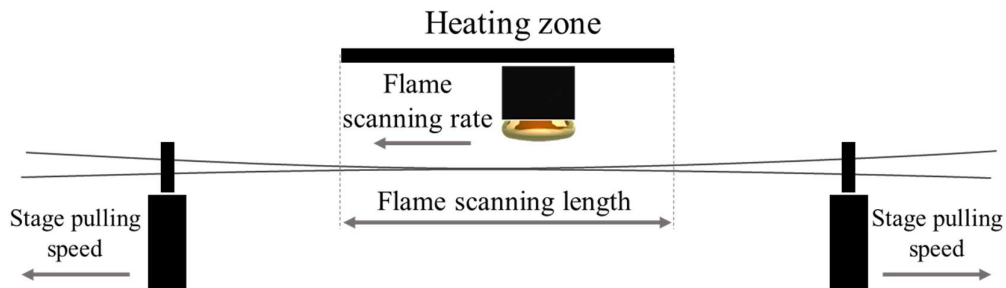


FIG. 2.1. Schematic diagram of the fibers' coupling process.

Typically, the process occurs at a steady temperature lying in the range of 1200-1900°C, at which the viscous sintering of the fibers may be regarded as the motion of an incompressible Newtonian fluid driven by surface tension [1] and damped by viscous dissipation forces. Although the system under consideration is 3D in practice, the fiber coupling process can be approximated by a transient quasi-3D model. The third axial direction along the tapered coupler is replaced by a series of discrete axial cross-sections of different areas. This approximation is acceptable in the case of an isothermally heated zone, which is a good approximation for the flame scanning setup, as long as the pulling rate is much lower than the scanning rate. Each such cross-section comprises the local structure of the glass coupler whose shape had formed as the coupler was drawn

through the heated zone. As long as the pulling rate remains constant, each cross-section can be related to the discrete-time at which the coupler had formed and had remained “frozen” immediately after it had been drawn out of the hot zone.

The decrease of the cross-sectional area $A(t)$ taking place at time t , as a result of simultaneous heating and drawing out of the coupler in the heated zone is related to the constant pulling rate v_s and the flame scanning length l , by the following ordinary differential equation:

$$\frac{d}{dt} A(t) + \frac{2v_s}{l} A(t) = 0, \quad (2.1)$$

whose analytical solution provides an expression for the decrease with time in the cross-sectional area $A(t)$:

$$A(t) = A_0 e^{-\frac{2v_s t}{l}}, \quad (2.2)$$

where A_0 is the initial cross-sectional area of the fibers forming the coupler. The decrease in the cross-sectional area of the coupler can be formulated by introducing a volumetric sink q , defined as:

$$q = -\frac{2v_s \rho(\mathbf{x})}{l}. \quad (2.3)$$

Eq. (2.3) will be utilized in the following sections when describing the fluid dynamics of the fabrication process of fiber couplers.

It should be noted that the developed simulation tool can be straightforwardly adjusted for configurations including non-uniform flame scanning. In this case, the distributed volumetric sink and the silica viscosity should be evaluated separately for each cross-section of the full 3D model. Afterwards, the time evolution of each cross-section can be resolved again by 2D analysis. This kind of simulation will be the focus of our future studies.

2.1 Governing equations

Consider two incompressible viscous fluids A and B confined by a rectangular domain, where the fluid B surrounds fluid A , and the two fluids are

separated by a sharp closed interface Γ parameterized by $\mathbf{X}(s,t)$, as shown in Fig. 2.2. In the context of the present study, fluid A is related to the viscous fused silica and represents the cross-section of the fiber coupler, whereas fluid B is related to the surrounding air.

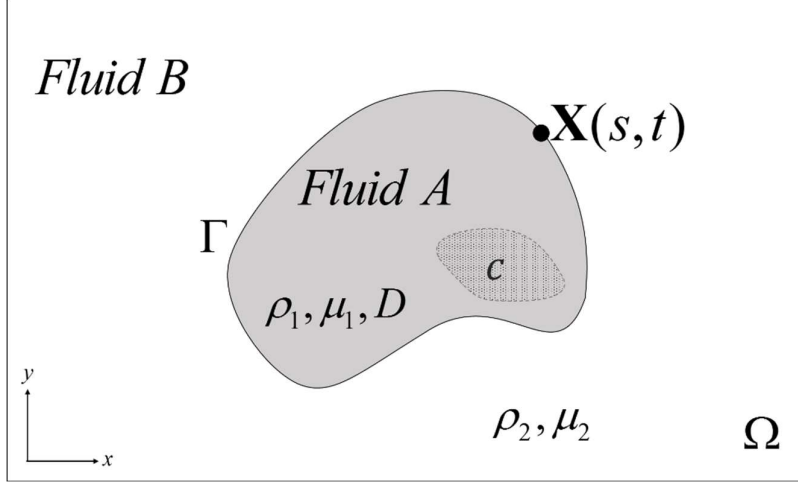


FIG. 2.2 Schematic representation of a two-phase flow configuration.

The two fluids have different densities and viscosities represented by $\rho_{1,2}$ and $\mu_{1,2}$, respectively. Fluid A is enriched with dopants to provide the requisite optical characteristics. The concentration distribution of the dopants c is controlled by convection and a constant diffusion coefficient \tilde{D} , and it is assumed that there is no diffusion between fluids A and B . Three equations govern the fluid dynamics of the described system, namely, the continuity, NS, and the dopant concentration convection-diffusion equations:

$$\rho(I)\nabla \cdot \mathbf{u} = q, \quad (2.4)$$

$$\rho(I)\left(\frac{\partial \mathbf{u}}{\partial t} + \mathbf{u} \cdot \nabla \mathbf{u}\right) = -\nabla p + \nabla \cdot \left(\mu(I)(\nabla \mathbf{u} + \nabla^T \mathbf{u})\right) + \frac{1}{3}\mu(I)\nabla(\nabla \cdot \mathbf{u}) + \mathbf{f} + \rho(I)g\bar{e}_y, \quad (2.5)$$

$$\frac{\partial c}{\partial t} + (\mathbf{u} \cdot \nabla)c = \tilde{D}\nabla^2 c, \quad (2.6)$$

where $\mathbf{u}(u,v)$, p , c , t , \mathbf{f} , and q represent the velocity, pressure, dopant concentration, time, surface tension force density and volumetric mass source,

respectively. \bar{e}_y is a unit vector in the direction which is opposite to that of the gravity force and g is the gravitational acceleration.

Note that because of the spatio-temporal variation of the viscosity, the governing equations (2.4-2.6) are presented and then solved in dimensional form. (This approach also subsequently facilitates the calibration and fine-tuning of the developed numerical methodology to the experiments.) Nonetheless, all the validation studies and the further post-processing of the obtained results are rendered dimensionless.

The indicator function, $I(\mathbf{x}, t)$ [41], is a non-dimensional scalar field, whose values lie within the range $I \in [0, 1]$. The indicator function is used for representing the spatial distribution of the material properties $[\rho(I), \mu(I)]$, and is used to smear their discontinuity in the vicinity of the sharp interface Γ separating the two fluids. We now define the gradient of the indicator function as:

$$\nabla I(\mathbf{x}, t) = \int_{\Gamma} \mathbf{n}(\mathbf{X}(s, t)) \delta^2(\mathbf{x} - \mathbf{X}(s, t)) ds, \quad (2.7)$$

where $\mathbf{n}(\mathbf{X}(s, t))$ is a unit vector normal to the interface Γ at point $\mathbf{X}(s, t)$ parameterized by $0 \leq s \leq L$ (L is the total length of the interface). The values of I are obtained by solving Poisson's equation:

$$\Delta I(\mathbf{x}, t) = \nabla \cdot \int_{\Gamma} \mathbf{n}(\mathbf{X}(s, t)) \delta^2(\mathbf{x} - \mathbf{X}(s, t)) ds, \quad (2.8)$$

where the 2D convolution function δ^2 is obtained by multiplication of two one-dimensional (1D) discrete Dirac delta functions d of the form:

$$d(r) = \begin{cases} \frac{1}{3\Delta r} \left(1 + \sqrt{-3\left(\frac{|r|}{\Delta r}\right)^2 + 1} \right) & \text{for } |r| \leq 0.5\Delta r, \\ \frac{1}{6\Delta r} \left(5 - 3\frac{|r|}{\Delta r} - \sqrt{-3\left(1 - \frac{|r|}{\Delta r}\right)^2 + 1} \right) & \text{for } 0.5\Delta r \leq |r| \leq 1.5\Delta r, \\ 0 & \text{otherwise,} \end{cases} \quad (2.9)$$

introduced by Roma et al. [27] and verified by [39, 48, 51, 52, 53, 54]. Here, Δr is the cell width in the r direction. Following the guidelines formulated by Tryggvason et al. [23], Eq. (2.8) was solved by the SOR method. The iterations were only performed on points close to the interface (typically two grid cells in each direction, which encloses the field of influence of the discrete Dirac delta function defined by Eq.(2.9), leaving points away from the interface unchanged. The procedure made it possible to precisely keep the correct values of the density and the viscosity fields away from the interface, separating between the phases. In addition, to prevent small over- and undershoots which can emerge near the interface when simulating the two-phase flows characterized by high density and viscosity ratios, a simple filtering was applied while iterating the $I(\mathbf{x}, t)$ values.

The obtained values of $I(\mathbf{x}, t)$ are then utilized to update the spatio-temporal variation of the ρ and μ fields:

$$[\rho, \mu](I(\mathbf{x}, t)) = [\rho_1(t), \mu_1(t)] + ([\rho_2(t), \mu_2(t)] - [\rho_1(t), \mu_1(t)])I(\mathbf{x}, t) \quad .(2.10)$$

The surface tension force density $\mathbf{f}(\mathbf{x}, t)$, appearing in the right-hand side (RHS) of Eq. (2.5), is related to the local curvature of the interface $\frac{\partial^2 \mathbf{X}(s, t)}{\partial s^2}$ as:

$$\mathbf{f}(\mathbf{x}, t) = \int_{\Gamma} \sigma \frac{\partial^2 \mathbf{X}(s, t)}{\partial s^2} \delta^2(\mathbf{x} - \mathbf{X}(s, t)) ds, \quad (2.11)$$

where σ is the surface tension coefficient.

2.1.1 Discretization in time and space

The time derivative in the unsteady momentum and the diffusion equations is approximated by a second-order backward differentiation:

$$\frac{\partial \psi^{n+1}}{\partial t} = \frac{3\psi^{n+1} - 4\psi^n + \psi^{n-1}}{2\Delta t} + O(\Delta t^2) . \quad (2.12)$$

In the momentum (2.5) and the diffusion (2.6) equations, the linear terms of diffusion and surface tension forces are treated implicitly, while convective nonlinear terms are treated explicitly and moved to the RHS of the corresponding equations. Due to explicit advancement of the nonlinear terms, the overall scheme is subjected to the restrictions in the size of the time steps. Thus, the time

increments must satisfy the usual Courant number criterion, which is defined in explicit schemes [55]:

$$C_x = |u| \Delta t / \Delta x \leq 1.0, C_y = |v| \Delta t / \Delta y \leq 1.0. \quad (2.13)$$

Also, when non-zero values of the dynamic viscosity and the molecular diffusivity are used, the momentum and the diffusion equations do not diffuse more than one cell in one time step due to stability considerations:

$$(\mu, D) \Delta t \left[1 / (\Delta x)^2 + 1 / (\Delta y)^2 \right] \leq \frac{1}{2}. \quad (2.14)$$

In a number of benchmark numerical tests [56, 41], in cases where discretization had h grid cells in the shortest direction ($\Delta x = 1/h$), the time step was $\Delta t = h/16$.

The finite volume approach was used for the spatial discretization performed on a staggered grid [57], as shown in Fig. 2.3. The staggered grid was introduced by Harlow and Welch [58] for the 'Marker And Cell' method, and has been used extensively in computational fluid mechanics ever since. There are two main reasons why the staggered grid characterized by an offset in the location of the different fields of the problem is widely used instead of a co-located grid, where all the fields are located at the same points. The first reason is related to the accuracy of the discretization. By using a staggered-grid, the pressure gradient is computed as the difference between the adjacent points. In contrast, when the calculation is performed on a co-located grid, the pressure gradient is evaluated by points distant from each other by $2\Delta x$ or $2\Delta y$. The second reason is that discretization on a staggered grid naturally makes it possible to keep the conservative form of the governing equations. At the same time, the terms of advection and the derivative of viscosity in the momentum equations require some extra manipulations for accurate formulation.

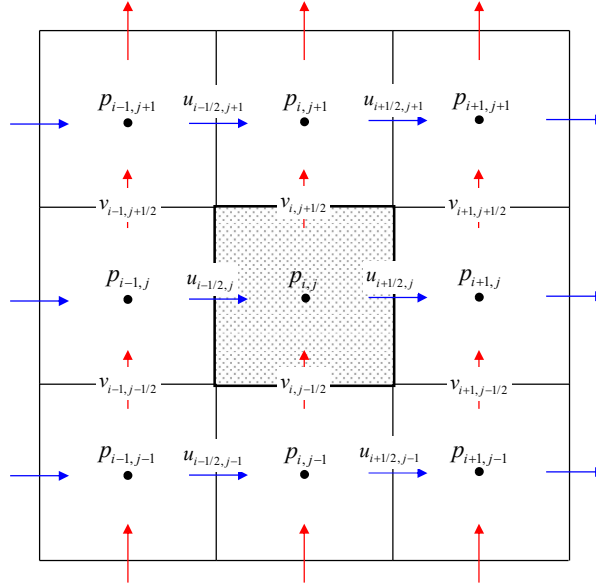


FIG. 2.3 Control volume for the pressure field – staggered grid arrangement.

2.2 Numerical methods

Direct numerical simulations (DNS) are widely used for single-phase flows in large time and length scales, and enable solving a wide range of problems. However, the use of DNS for multi-phase flows is less common [33]; therefore, developing such a tool can make a considerable contribution to the field.

In this section, the IB method was adapted for the simulation of two- and multi-phase fluid flows, and is presented.

2.2.1 Immersed Boundary method

The IB method was originally proposed by Peskin in 1977 [26]. The method was developed to accurately simulate the interaction of blood flow in the heart, and since then, it has been widely utilized for the simulation of flow in many biological problems [25]. The main idea of this method is to use the Eulerian fixed grid, together with Lagrangian markers representing the IB. In our research, we use the IB method for calculating the surface tension term, while the velocity and pressure fields are calculated on the Eulerian grid. The interaction between these two grids is achieved by regularizing the surface tension force from Lagrangian markers to adjacent locations on the Eulerian grid, and by interpolating the Eulerian velocity fields to the nearby Lagrangian markers. Both operations are

implemented by utilizing the same discrete Dirac delta function (Eq. (2.9)). By applying the delta function, we impose the contribution of the distributed force of the boundary as a function of a non-dimensional distance r of the Lagrangian marker to adjacent locations on the Eulerian grid.

It should be noted that, as a result of solving the continuity equation on the Eulerian grid, the IB method utilized for the solution of the proposed problem does not explicitly provide the volume conservation of both phases. For this reason, Li [41] proposed a simple area-preserving scheme for two-phase fluids by performing further iterations to correct for mass conservation. In contrast, our method manages to preserve mass conservation with no need for extra iterations. Extensive details are presented in the next section.

2.2.2 The numerical methodology

The numerical methodology utilized in the present study is based on the IB method, specifically developed to simulate two-phase immiscible flows [52]. In the developed methodology, the enforcing surface tension density \mathbf{f} is treated implicitly, and serves as a Lagrange multiplier, applied to enforce the kinematic constraint of the immiscibility of the two fluids to preserve the sharp interface between the two phases.

The developed methodology is embedded into the generic incompressible NS solver, based on full pressure-velocity coupling [50]. The position of the interface is updated by employing the interface-tracking approach [23, 24]. Following Eq. (2.11), implicit treatment of the surface force density \mathbf{f} leads to the introduction of additional unknowns, $\left(\frac{\partial^2 X}{\partial s^2}, \frac{\partial^2 Y}{\partial s^2}\right)$, which requires the addition of supplementary equations to achieve closure of the overall set of equations:

$$\left(\frac{\partial^2 \mathbf{X}_l}{\partial s^2}\right) = \frac{\left(\mathbf{X}_{l+1}^{n+1} - 2\mathbf{X}_l^{n+1} + \mathbf{X}_{l-1}^{n+1}\right)}{(\Delta s)^2}, \quad (2.15)$$

$$\mathbf{X}_l^{n+1} = \mathbf{X}_l^n + \Delta t \int_{\Omega} \mathbf{u}^{n+1} \delta^2(\mathbf{X}_l^n - \mathbf{x}) dx dy. \quad (2.16)$$

Substitution of \mathbf{X}_{l-1}^{n+1} , \mathbf{X}_l^{n+1} and \mathbf{X}_{l+1}^{n+1} defined by Eq. (2.16) into Eq. (2.15)

and moving all the terms known from the previous time step to the RHS yields:

$$\frac{\Delta t \int_{\Omega} \mathbf{u}^{n+1} \left[\delta^2(\mathbf{X}_{l+1}^n - \mathbf{x}) - 2\delta^2(\mathbf{X}_l^n - \mathbf{x}) + \delta^2(\mathbf{X}_{l-1}^n - \mathbf{x}) \right] dx dy}{(\Delta s)^2} - \left(\frac{\partial^2 \mathbf{X}_l}{\partial s^2} \right) =$$

$$- \frac{\mathbf{X}_{l+1}^n - 2\mathbf{X}_l^n + \mathbf{X}_{l-1}^n}{(\Delta s)^2} \quad (2.17)$$

The system of equations (2.4),(2.5) and (2.17) can now be written in block-matrix form as

$$\begin{bmatrix} H_u & H_{uv} & -\nabla_p^x & \sigma \delta^2(\mathbf{X}(s, t^n) - \mathbf{x}) & 0 \\ H_{vu} & H_v & -\nabla_p^y & 0 & \sigma \delta^2(\mathbf{X}(s, t^n) - \mathbf{x}) \\ \nabla_u^x & \nabla_v^y & 0 & 0 & 0 \\ IC_x & 0 & 0 & -1 & 0 \\ 0 & IC_y & 0 & 0 & -1 \end{bmatrix} \begin{bmatrix} u^{n+1} \\ v^{n+1} \\ p \\ \left(\frac{\partial^2 X}{\partial s^2} \right) \\ \left(\frac{\partial^2 Y}{\partial s^2} \right) \end{bmatrix} = \begin{bmatrix} RHS_u^{n-1,n} \\ RHS_v^{n-1,n} \\ RHS_s^n \\ RHS_X^n \\ RHS_Y^n \end{bmatrix}, \quad (2.18)$$

where $H = \nabla \cdot (\mu(I)(\nabla + \nabla^T)) + \frac{1}{3}\mu(I)\nabla(\nabla \cdot) - \frac{3\rho(I)}{2\Delta t}\mathbf{I}$ are Helmholtz operators acting on the u and v velocity components, \mathbf{I} is the identity matrix, and ∇^x ∇^y are the first derivatives in the x and y directions, respectively. IC is the ‘Interface Curvature’ operator appearing as the first term of Eq. (2.17). The RHS is defined as:

$$RHS_{u,v} = \rho(I) \left[(\mathbf{u} \cdot \nabla) \mathbf{u} - \frac{2}{\Delta t} \mathbf{u} \right]^n + \frac{1}{2\Delta t} \mathbf{u}^{n-1}, \quad (2.19)$$

$$RHS_{X,Y} = - \frac{\mathbf{X}_{s+1}^n - 2\mathbf{X}_s^n + \mathbf{X}_{s-1}^n}{(\Delta s)^2}, \quad (2.20)$$

$$RHS_s = \begin{cases} -\frac{2v_s}{l} e^{-\frac{2v_s \Delta t}{l}} & \text{within fluid A,} \\ 0 & \text{otherwise} \end{cases} \quad (2.21)$$

All the discrete operators were obtained by applying a second-order backward finite difference scheme for the temporal discretization, and utilizing the standard second-order conservative finite volume method [36] for the

staggered grid spatial discretization. Additionally, all the linear terms were treated implicitly, and all the nonlinear terms were treated explicitly and appear in the RHS.

The solution of the equation system (2.18) is based on an LU factorization of the sparse matrix, built for the entire computational domain. The LU factorization is carried out by a direct Multifrontal Massively Parallel Solver (MUMPS) [59, 60] and has to be performed at every time step as a result of varying material properties in the operator H . The successive calculation of the velocity and pressure fields is implemented by the backward substitution procedure, also realized for sparse triangular L and U matrices. Due to efficient utilization of the matrix sparsity, both LU factorization and back substitution procedures are relatively fast. The boundary conditions are of the Dirichlet, Neumann, and periodic types, each applied in accordance with the specific problem.

The convection-diffusion equation (Eq. (2.6)) was solved separately from all the other equations by using the velocity field from the previous time sub-step. The equation was solved only for the fluid domain A , with a zero gradient boundary condition on the interface Γ (see Fig. 2.2).

To conclude, each computational time step consisted of three main sub-steps: The first one was the solution to Poisson's equation, given by Eq.(2.8). The obtained indicator function $I(\mathbf{x}, t)$ was then used in Eq.(2.10) to identify the spatial distribution of the μ and ρ fields. In the second sub-step, the system of equations (2.18) was solved implicitly by MUMPS [59, 60] to obtain the fully coupled velocity and pressure fields. Finally, in the third step, diffusion Eq. (2.6) was solved to obtain the concentration of dopants c , under the assumption of one-way coupling (i.e., no dependence of the flow ρ and μ fields on the concentration of dopants), and the interface position was updated by utilizing Eq. (2.16). The whole procedure was then repeated for the next time step (see Fig 2.4).

Note that for the case of zero concentration, it is possible to skip the convection-diffusion equation (Eq. (2.6)) and to update the interface directly after the second step.

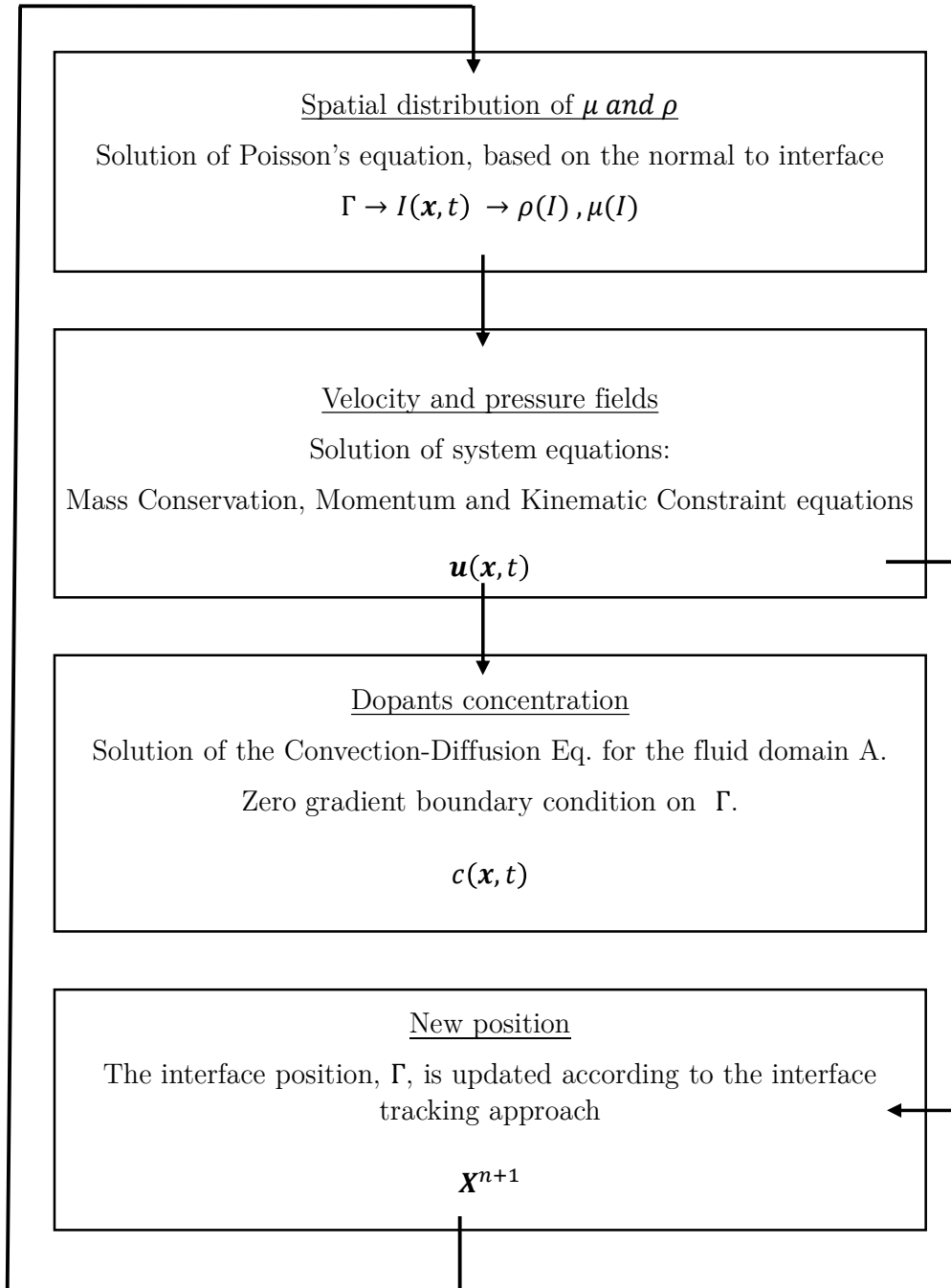


FIG. 2.4 Block diagram of the computational time step.

Chapter 3: Validation study

In order to broadly verify the developed method for a wide range of applications, four benchmark problems for incompressible two-phase flows were solved. The flows under consideration were driven by different mechanisms, namely; buoyancy, shear, and surface tension forces. The benchmark problems were solved non-dimensionally, where the non-dimensional equations were obtained by using the characteristic scales $D = 2\sqrt{S/\pi}$ for the length (where S is the area of fluid A), U for the velocity (where U is the characteristic velocity of the specific flow configuration), $t = D/U$ for the time, and $p = \mu_{\min} U/D$ for the pressure field. The mass density and the dynamic viscosity fields were scaled by the corresponding minimum values of either of the two fluids, ρ_{\min} and μ_{\min} . The non-dimensional groups determining the two-phase flow under consideration are the Reynolds (Re), Weber (We) and Froude (Fr) numbers, defined as

$$Re = \frac{\rho_{\min} UD}{\mu_{\min}}, \quad We = \frac{\rho_{\min} U^2 D}{\sigma}, \quad Fr = \frac{U}{\sqrt{gD}} \quad .(3.1)$$

The first and second benchmark problems consider the flow of a circular bubble rising within a fluid of higher density due to buoyancy forces [30, 56, 61]. In general, both fluids can also have different viscosities. Under the action of buoyancy forces, the bubble accelerates while rising up, until it reaches its terminal velocity. Similarly to the first benchmark problem, the second configuration also comprises a circular bubble rising within a fluid of higher density, with the only difference being that in this case, the flow is characterized by higher values of density and viscosity ratios, which eventually leads to break-up of the rising bubble. The third benchmark is the shape evolution of a drop under pure shear stress [41, 62, 63]. A circular drop of a certain liquid is submerged into a pure shear flow of another liquid. Both liquids have different viscosities. As a result of shear forces, the submerged circular drop undergoes

shape deformation. The fourth benchmark is known as the disc relaxation problem [41, 64]. A drop of a certain fluid with an initial rosette shape is submerged in another fluid of different viscosity. As a result of surface tension forces between the two phases, the rosette-shape drop undergoes complex deformations until it eventually converges to a circular shape. The results of our simulations were compared both qualitatively and quantitatively to the data available from the literature [65, 66, 67] for different Reynolds, Weber, and Froude numbers. A detailed comparison between the results was published [52], and is presented in the following section.

3.1 Test case 1 - Rising bubble without break-up

This benchmark focuses on the dynamics of a deformable liquid bubble submerged in a cavity filled with another fluid of higher density. This flow has been thoroughly studied both experimentally [68] and numerically [30, 56, 61, 69, 70]. The most comprehensive quantitative results are due to the review of Hysing et al. [56], which presents a comparison between the time evolutions of the circularity, the position of the center of mass, and the vertical component of the velocity of the rising bubble's center of mass as defined in Eq. (19). This data was independently obtained by three research groups, each utilizing its own numerical methodology (consult Ref. [56] for more details).

The buoyant dynamic of an initially circular rising bubble of diameter D is considered. The bubble is initially placed at point $[D, D]$ within a $[2D \times 4D]$ rectangular domain, as shown in Fig. 3.1.

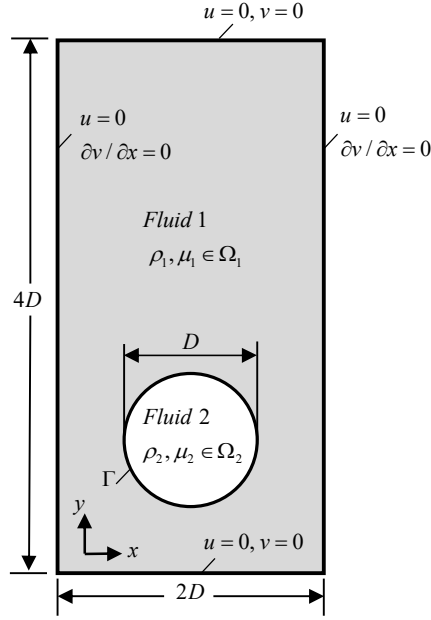


FIG. 3.1 – Initial configuration and boundary conditions of rising bubble test flow.

The boundary conditions are set as:

$$\begin{aligned}
 u(x=0, y) &= u(x=2D, y) = 0, \\
 u(x, y=0) &= u(x, y=4D) = 0, \\
 \frac{\partial v}{\partial x}(x=0, y) &= \frac{\partial v}{\partial x}(x=2D, y) = 0, \\
 v(x, y=0) &= v(x, y=4D) = 0,
 \end{aligned} \tag{3.2}$$

In addition, a single Dirichlet point for the pressure field, $p = 0$, was set in the corner of the computational domain. The values of physical properties and operating conditions governing the flow under consideration are specified in Table 1.

Table 1 - The values of physical properties and operating conditions.

| ρ_1 | ρ_2 | μ_1 | μ_2 | D | g | σ | Re | We | Fr | ρ_1 / ρ_2 | μ_1 / μ_2 |
|----------|----------|---------|---------|-----|------|----------|-------|------|------|-------------------|-----------------|
| 1000 | 100 | 10 | 1 | 1 | 0.98 | 24.5 | 98.99 | 4 | 1 | 10 | 10 |

The center of mass of the rising bubble is a local quantity given by:

$$\mathbf{X}_C = (X_C, Y_C) = \frac{\int_{\Omega_2} \mathbf{x} dV}{\int_{\Omega_2} dV}, \tag{3.3}$$

where Ω_2 denotes the region occupied by the bubble.

Following Wadell [71], the bubble's ‘degree of circularity’ ϕ is defined in \mathbf{R}^2 as

$$\phi = \frac{P_a}{P_b} = \frac{\pi D_a}{P_b}, \quad (3.4)$$

where P_a is the perimeter of a circle with diameter D_a , which has an area equal to that of a bubble with perimeter P_b .

The rising velocity, \mathbf{U}_C , is defined as the mean velocity of the bubble:

$$\mathbf{U}_C = (U_C, V_C) = \frac{\int_{\Omega_2} \mathbf{u} dV}{\int_{\Omega_2} dV}. \quad (3.5)$$

To prove the grid independence of the results, the simulations were performed on four different grids with a time step of $\Delta t = h / 2$, where h corresponds to the grid step. Grid independence of the obtained results is favorably verified by indistinguishable differences between the final shapes of the bubble obtained at $t = 3$ on the two finest grids (see Fig. 3.2).

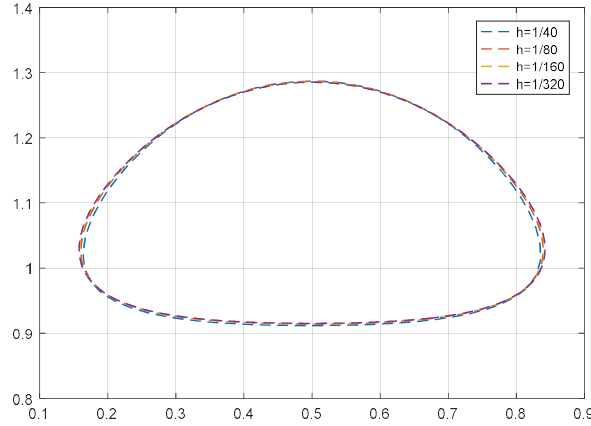


FIG 3.2 – Bubble shapes obtained on four different grids at time $t = 3$.

In addition, it can be clearly recognized that the bubble shape obtained at time $t = 3$ on the finest grid is in excellent agreement with the corresponding results reported in Hysing et al. [56] (see Fig.3.3). Mass conservation of the bubble is next verified by comparison between the initial and the final areas of the bubble. It can be seen that for all the grids, the mass lost does not exceed 0.35% of the initial mass, as summarized in Table 2.

Table 2. Mass discrepancy (%) at $t=3$ in test case 1.

| h | 1/40 | 1/80 | 1/160 | 1/320 |
|------------------|--------|--------|--------|--------|
| Mass leakage [%] | 0.3364 | 0.0917 | 0.0560 | 0.0204 |

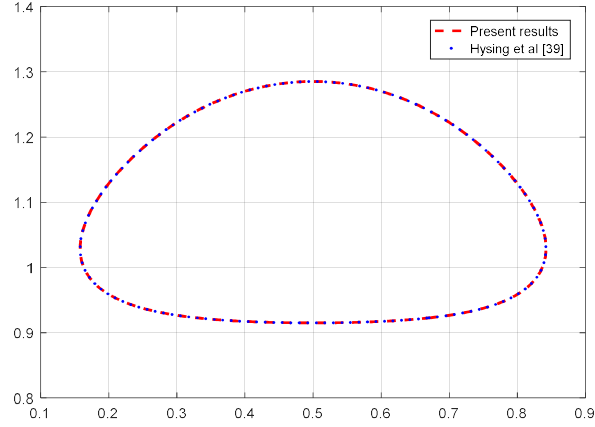


FIG. 3.3 – Bubble shapes obtained at final time ($t=3$): comparison between the present and the previously published results.

Figs. 3.4, 3.5, and 3.6 compare between the present and the previously reported time evolutions of the circularity, the Y-axis position, and the V_c velocity component of the bubble’s center of mass, respectively. All the results were calculated on the grid characterized by $h = 1 / 160$ with $\Delta t = h / 16$.

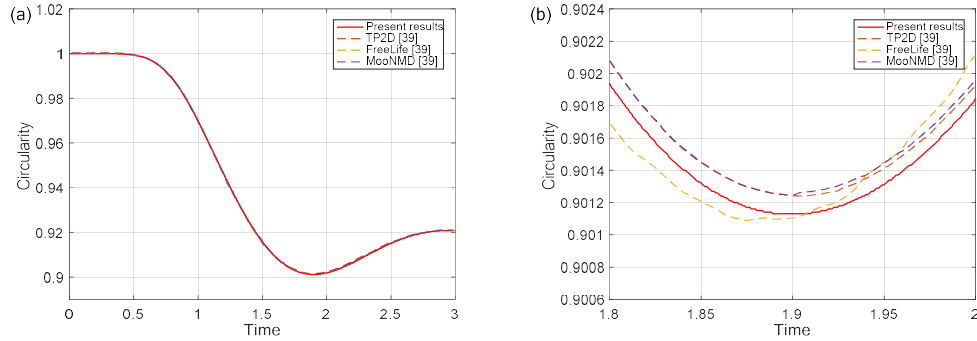


FIG. 3.4 – Time evolution of the circularity values: (a) the whole-time history; (b) close-up view around the time $t=1.9$.

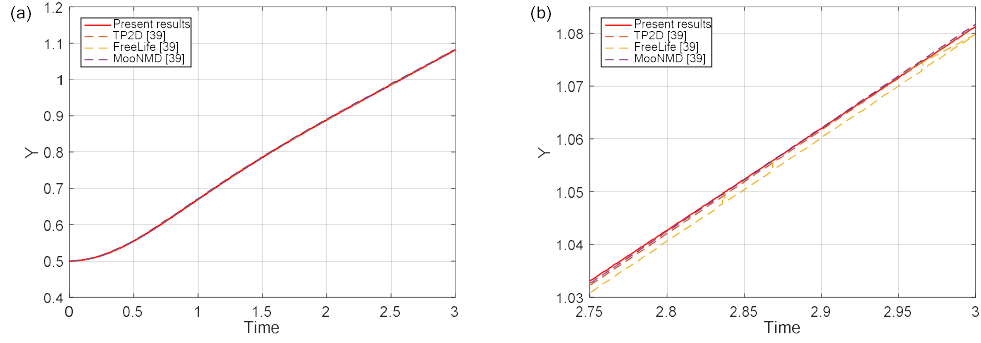


FIG. 3.5– Time evolution of the Y position of the center of mass: (a) the whole-time history; (b) close-up view around the time $t=2.9$.

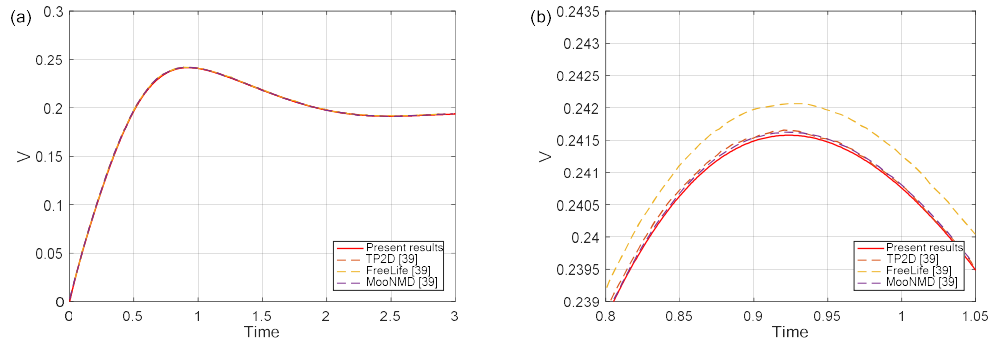


FIG. 3.6– Time evolution of the rise velocity: (a) the whole history; (b) close-up view around the time $t=0.9$.

In addition, Table 3 presents a quantitative comparison between the corresponding instantaneous values of the global minima of circularity, global maxima of rising velocity and vertical position of the center of mass at $t = 3$.

It can be clearly recognized that all the presently obtained characteristics are very close to the corresponding previously obtained results for the entire range of time instances. The maximal discrepancy between all the flow characteristics does not exceed 0.04%. The maximal deviation between the circularities is observed around their global minima (close to the time $t = 1.9$), characterizing the most significant deformation of the shape of a rising bubble compared to its initially circular geometry. From this point on, the circularity smoothly increases until finally attaining its asymptotic value that indicates that the bubble has reached its terminal velocity. The fact that the bubble has reached its terminal velocity is also confirmed by noting a constant slope of the time evolution of the Y coordinate around time $t = 2.9$ (see Fig. 3.5-b).

Table 3. Global minima values of circularity with corresponding incident times, global maxima values of rising velocity and final vertical position of the center of mass.

| | Present method | TP2D | FreeLife | MooNMD |
|-----------------------------|----------------|--------|----------|--------|
| ϕ_{\min} | 0.9011 | 0.9013 | 0.9011 | 0.9013 |
| $t \mid \phi = \phi_{\min}$ | 1.9000 | 1.9041 | 1.8750 | 1.9000 |
| V_{\max} | 0.2416 | 0.2417 | 0.2421 | 0.2417 |
| $t \mid V = V_{\max}$ | 0.9232 | 0.9213 | 0.9313 | 0.9239 |
| $Y(t = 3)$ | 1.0813 | 1.0813 | 1.0799 | 1.0817 |

It is remarkable that the value of the terminal velocity is lower than the value of the global velocity maxima observed at $t \approx 0.9$ by about 10% (see Fig. 3.6-b). Increasing the vertical velocity of the bubble is followed by enhanced deformation of the bubble shape, which results in a moderate deceleration of the bubble until it reaches its terminal velocity.

3.2 Test case 2 - Rising bubble undergoing break-up

The aim of this simulation is to demonstrate that the developed methodology is also capable of simulating immiscible two-phase flows with multiple separated boundaries. For this purpose, the rise of a 2D gas bubble with its subsequent break-up in a quiescent liquid is considered. The geometry and boundary conditions of the flow are the same as for test case 1. The values of physical properties utilized in the present simulations are equivalent (subject to appropriate rescaling) to those used in the previous studies [65, 66, 67], as detailed in Table 4.

Table 4 - The values of physical properties and operating conditions utilized in test case 2.

| Re | We | Fr | ρ_1 / ρ_2 | μ_1 / μ_2 |
|--------|------|------|-------------------|-----------------|
| 120.83 | 2.6 | 1 | 40 | 83.33 |

Unfortunately, the breaking process cannot be directly captured only by the solution of the NS equations with the subsequent Euler integration of the two-phase interface governed by Eq. (2.16). Explicit modeling of the bubble

break-up is required. In the present study, we adopt an assumption that the breaking process is followed by the formation of a deformed neck, which is thinned by the dynamic local pressure. This scenario is realistic for many physical systems, for example, for the microfluidic dynamics of two-phase immiscible flow in T-junctions [72, 73, 74], and is favorably applied here to simulate bubble break-up in buoyant and pure shear flows. A schematic of bubble break-up modeling is shown in Fig. 3.7. The distance between all points of the body, with the exception of a pair of points in the immediate neighborhood of the break-up, is evaluated for every point of the immersed surface at each computational time step.

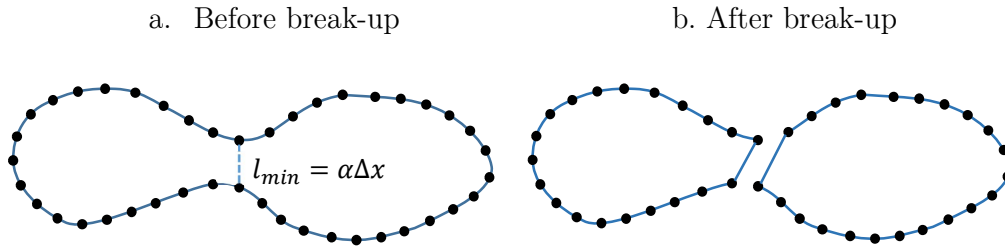


FIG. 3.7. Schematic bubble break-up modeling.

Once the absolute minimal distance between any two points of the body l_{\min} is less than a given threshold $\alpha\Delta x$ (see Fig. (3.7-a)) the body is split into two parts (see Fig. (3.7-b)), where each part is treated as a separate body at the next computational time. In this study, the value of α was set in the range of $1 \leq \alpha \leq 1.5$, which corresponds to the grid size length and to the range of influence of the presently utilized discrete Delta function, respectively. Although the above splitting procedure could result in a certain loss of mass, it was verified that for the chosen range of α values the mass discrepancy of a single break-up phenomenon was within the discretization error of the numerical scheme¹. After

¹ The described break-up procedure should be empirically rescaled to preserve mass if multiple break-up phenomena take place.

the splitting, Lagrangian points of each newly formed body were redistributed to preserve an even spacing with the distance approximately equal to the size of the Eulerian grid.

The time evolution of the rising initially cylindrical bubble simulated for the physical parameters listed in Table 4 is shown in Fig. 3.8 for $t = 1.5, 3, 4.5, 6$. Mass conservation of the rising bubble was verified at all the time instances (see Table 5). It can be seen that the maximum mass loss does not exceed 0.15% of the initial bubble mass. The instantaneous shape of the bubble is superimposed with contours corresponding to the absolute values of the velocity vector, $|\mathbf{u}|$. The obtained results are in acceptable agreement with the results of Gaudlitz and Adams [65], Wang et al. [66], and Archer and Bai [67] for $t = 1.5$ and $t = 3$. For these time instances, the symmetry of the flow relative to the vertical centerline is preserved. It can also be seen that at $t = 4.5$ the drop has already undergone its primary and secondary break-ups, followed by the slight symmetry breaking in the shapes of the major and four small pinched off bubbles. The crescent thin arms from both sides of the bubble continue to elongate even more as the bubble rises. The flow dynamics after the break-up is somewhat different from that observed in the previous studies [65, 66, 67] based on the LS method. One of the reasons for the observed discrepancies could be attributed to the different grid resolutions: the present results were obtained on a 320×640 grid, while all the previously reported results were obtained on a rather dense 40×80 grid. It should be noted that when such a dense grid was applied for the present methodology, it provided inconclusive results, which can be seen as a drawback of the FT approach compared to its LS counterpart. On the other hand, the results obtained by the LS method can be under resolved, which can result in mass conservation violation. An additional reason for the differences in the post break-up shapes of the bubbles could be due to the modeling of the break-up process adopted in the present study, which can be further modified by various fine-tuning strategies to better comply with existing experimental or numerical results. Recalling that the main purpose of this simulation was to demonstrate the capability of the

developed algorithm to handle multiple separated boundaries, the development of such fine-tuning strategies was beyond the scope of the present study.

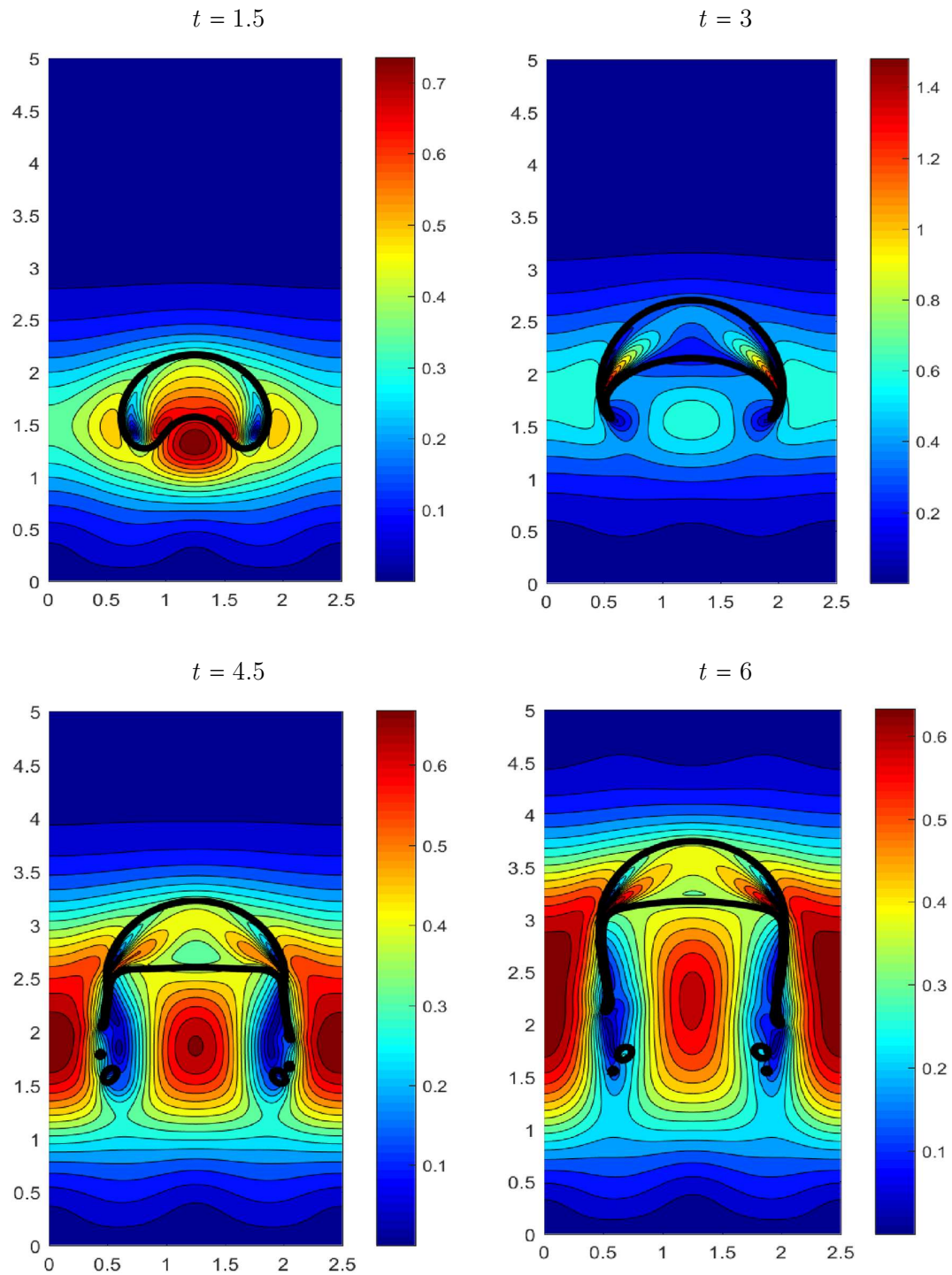


FIG. 3.8. Time evolution of the rising initially cylindrical bubble obtained on a 320×640 grid for the value of $\alpha=1.5$ and zero initial velocity. The initial position of the bubble center was $(1.25, 1.0)$. The colors correspond to absolute values of the velocity vector, $|\mathbf{u}|$.

Table 5. Mass discrepancy (%), calculated at every time instance in test case 2.

| Time | 1.5 | 3 | 4.5 | 6 |
|------------------|--------|--------|--------|--------|
| Mass leakage [%] | 0.1664 | 0.2858 | 0.1141 | 0.1346 |

3.3 Test case 3 - Drop under shear flow

The initial state of the problem is given in Fig. 3.9. The circular drop submerged into fully developed Couette flow is subjected to pure shear stress, while the gravity force is neglected. Under the action of shear stresses, the flow undergoes deformation until the increasing surface tension forces equalize with the shear forces and the drop shape reaches equilibrium. The square box domain is of dimensions $[2D, 2D]$, and the center of the submerged circular drop with diameter D coincides with the geometrical center of the box (point $[D, D]$). Following the works of Kapil & Pozrikidis [63] and Chinyoka et al. [62], the simulations were performed for four different values of Reynolds number, $Re = 1, 10, 50$ and 100 , two values of viscosity ratio $\mu_2 / \mu_1 = 1$ and 10 , and two values of capillary number, $Ca = 0.2$ and 0.4 . Note that the capillary number relates between the viscous and surface tension forces and is defined in the present study as

$$Ca = \frac{We}{Re} = \frac{U \mu_{\min}}{\sigma}. \quad (3.6)$$

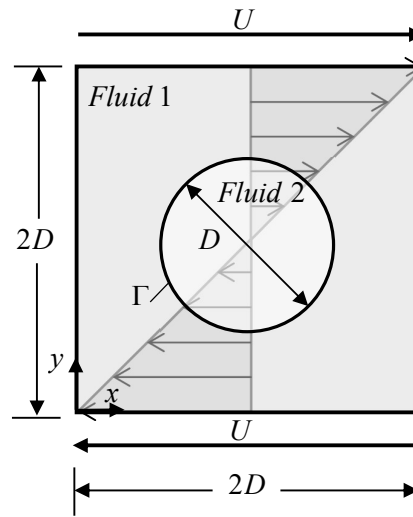


FIG. 3.9 – Initial state of the circular drop submerged into a fully developed Couette flow.

The boundary conditions applied in the above configuration are that the top and bottom walls of the cavity for all the velocity components are of the Dirichlet type:

$$\begin{aligned} u(x, y = 2D) &= -u(x, y = 0) = U, \\ v(x, y = 2D) &= v(x, y = 0) = 0 \end{aligned} \quad (3.7)$$

In addition, periodic boundary conditions were applied for the velocity and pressure fields in the horizontal, x , direction. A single Dirichlet point for the pressure field, $p = 0$, was set in the corner of the computational domain. The mesh grid $h = 1 / 300$ and time step $\Delta t = 10^{-4}$ were utilized in all the simulations.

A comparison between the present and the previously published data [62] for the drop shapes at steady state as a function of various values of operating conditions is presented in Fig. 3.10. An excellent agreement between the results is observed for the entire range of parameters. It can be seen that increasing the Ca number results in more pronounced elongation of the drop shape, which can be explained by the reduced surface tension force. In contrast, increasing the viscosity ratio leads to decreasing the deformation of the drop shape. The mass leakage calculated for all the configurations analyzed in test case 3 is summarized in Table 6 at the final time $t=3$. It can be seen that the maximal value of mass loss does not exceed 0.023% of the initial drop mass.

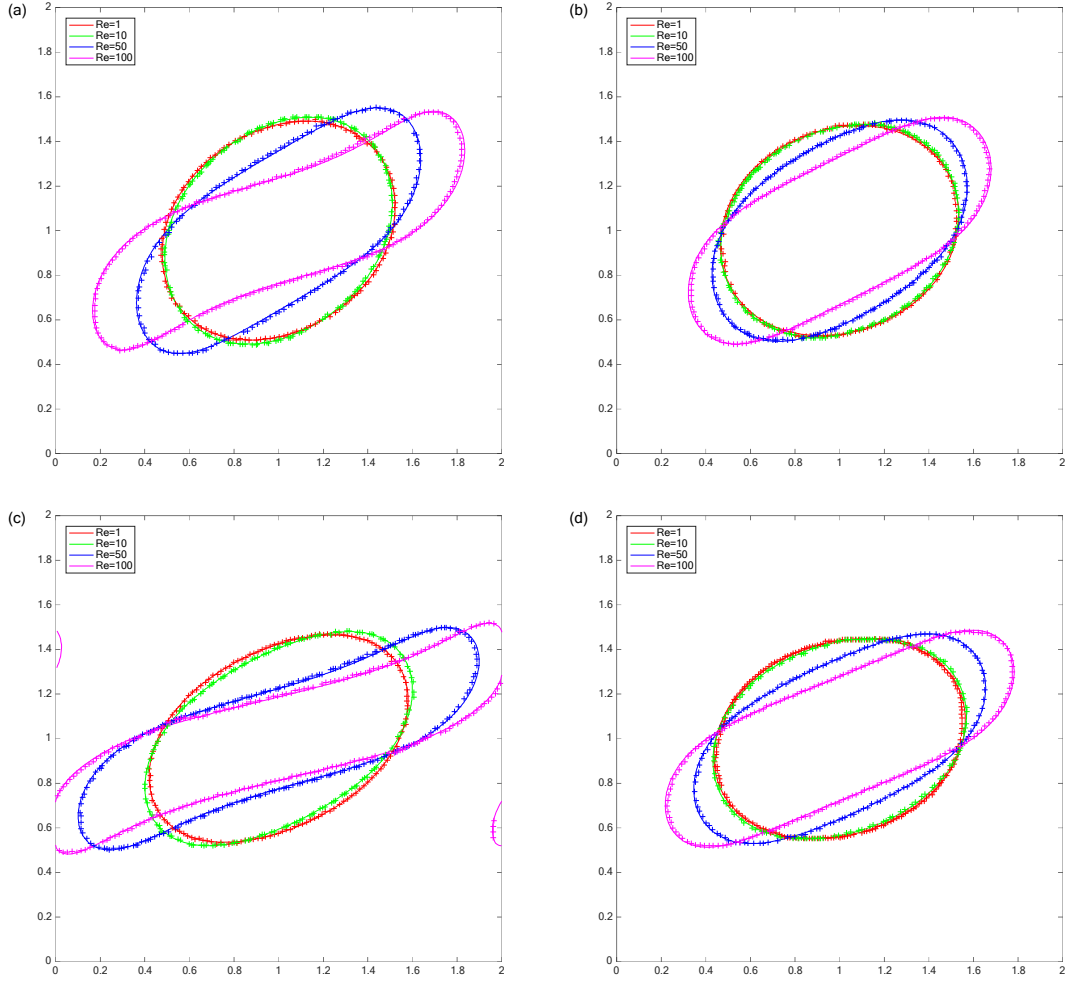


FIG. 3.10 - Drop shapes at $t=3$: (a) $Ca=0.2$, $\mu_r = 1$; (b) $Ca=0.2$, $\mu_r = 10$; (c) $Ca=0.4$, $\mu_r = 1$; and (d) $Ca=0.4$, $\mu_r = 10$. Plus markers – Chinyoka et al. [62] results, Lines – the present results.

Table 6. Mass discrepancy (%) at $t=3$ in test case 3.

| | $Ca = 0.2$ | | $Ca = 0.4$ | |
|------------|-------------|--------------|-------------|--------------|
| | $\mu_r = 1$ | $\mu_r = 10$ | $\mu_r = 1$ | $\mu_r = 10$ |
| $Re = 1$ | 0.0089 | 0.0038 | 0.0051 | 0.0038 |
| $Re = 10$ | 0.0089 | 0.0064 | 0.0051 | 0.0064 |
| $Re = 50$ | 0.0102 | 0.0178 | 0.0064 | 0.0166 |
| $Re = 100$ | 0.0102 | 0.0228 | 0.0064 | 0.0216 |

3.4 Test case 4 - Rosette shape

This benchmark investigates the dynamics of the relaxation of a rosette-shaped drop to a circular disc in a quiescent viscous liquid. In this configuration, the flow is driven by the surface tension forces, while the momentum of the flow is diffused by the viscosity of the fluid. Gravity is neglected. The initial configuration in this problem consists of a rosette-shaped drop. The center of the drop coincides with the center of a square cavity. The initial shape of the drop is defined by

$$\mathbf{X} = \begin{cases} X = D \cdot (0.5 + r \cos(\theta)) \\ Y = D \cdot (0.5 + r \sin(\theta)) \end{cases}, \quad 0 \leq \theta \leq 2\pi, \quad (3.8)$$

where $r = 0.25 + 0.1 \cos(n\theta)$ and n is the oscillation mode. Nonslip boundary conditions were applied at all the cavity walls. In addition, a single Dirichlet point for the pressure field, $p = 0$, was set in the corner of the computational domain. Following the study of Li et al. [41], the problem was studied for three different modes of $n = 3, 5$ and 8 , as shown in Fig. 3.11.

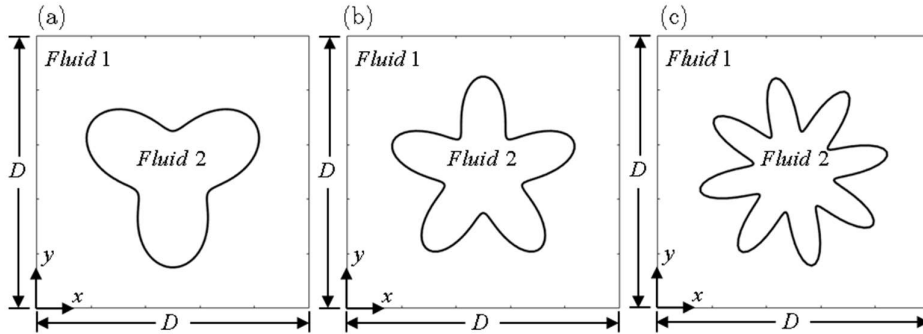


FIG. 3.11 – Initial configurations of rosette-shaped drop corresponding to: (a) $n=3$ modes; (b) $n=5$ modes; (c) $n=8$ modes.

Since neither the characteristic velocity, nor the Reynolds and Weber number values were specified in [42], the present simulations were carried out by solving dimensional NS equations on the computational domain $\Omega = (0,1) \times (0,1)$ with physical and geometrical parameters provided by [41], as detailed in Table 7.

Table 7. Physical and geometry parameters utilized in test case 4.

| ρ_1 | ρ_2 | μ_1 | μ_2 | D | σ |
|----------|----------|---------|---------|-----|----------|
| 1 | 1 | 0.01 | 0.01 | 1 | 130 |

The problem was solved on $h = 1 / 64, 128$ grids with $\Delta t = h / 16$. The time evolution of the rosettes is visualized by presenting the rosette shapes at various time instances in the range of $0 \leq t \leq 1$, as shown in Fig. 3.12. Lagrangian markers determining the instantaneous rosette shapes are superimposed with the corresponding rosette shapes reported in [41]. In agreement with the Li et al. study [41], all the three modes of the rosette drop relax to a disc shape at $t = 1$. However, in some instances, the presently obtained rosette shapes precede the corresponding shapes reported in [41]. Such a discrepancy, indicating a higher rate of momentum diffusion in our simulations, can be, apparently, a consequence of differences in the distribution of Lagrangian markers at each simulation instance. Contrary to the study of Li et al. [41], in which a constant number of Lagrangian markers is used for determining the two-phase interface, the presently developed methodology utilizes a varying number of Lagrangian markers, while preserving their even distribution over the interface. It can also be seen that higher modes are characterized by higher relaxation rates as a consequence of initially higher values of surface tension forces, which are proportional to the curvature of the interface separating both phases. Conservation of the area of the drop at each time step of the simulation comprises a critical criterion for verification of the developed approach, as it is dictated by the flow incompressibility. It was also verified (see Table 8) that for all simulations, the maximal discrepancy in the area did not exceed 0.5% for $h=1/64$ and 0.21% for $h=1/128$.

Table 8. Mass discrepancy (%) at $t=0.5$ in test case 4.

| Mode | 3 | 5 | 8 |
|---------------|--------|--------|--------|
| $h = 1 / 64$ | 0.4437 | 0.4720 | 0.4900 |
| $h = 1 / 128$ | 0.2028 | 0.2170 | 0.2075 |

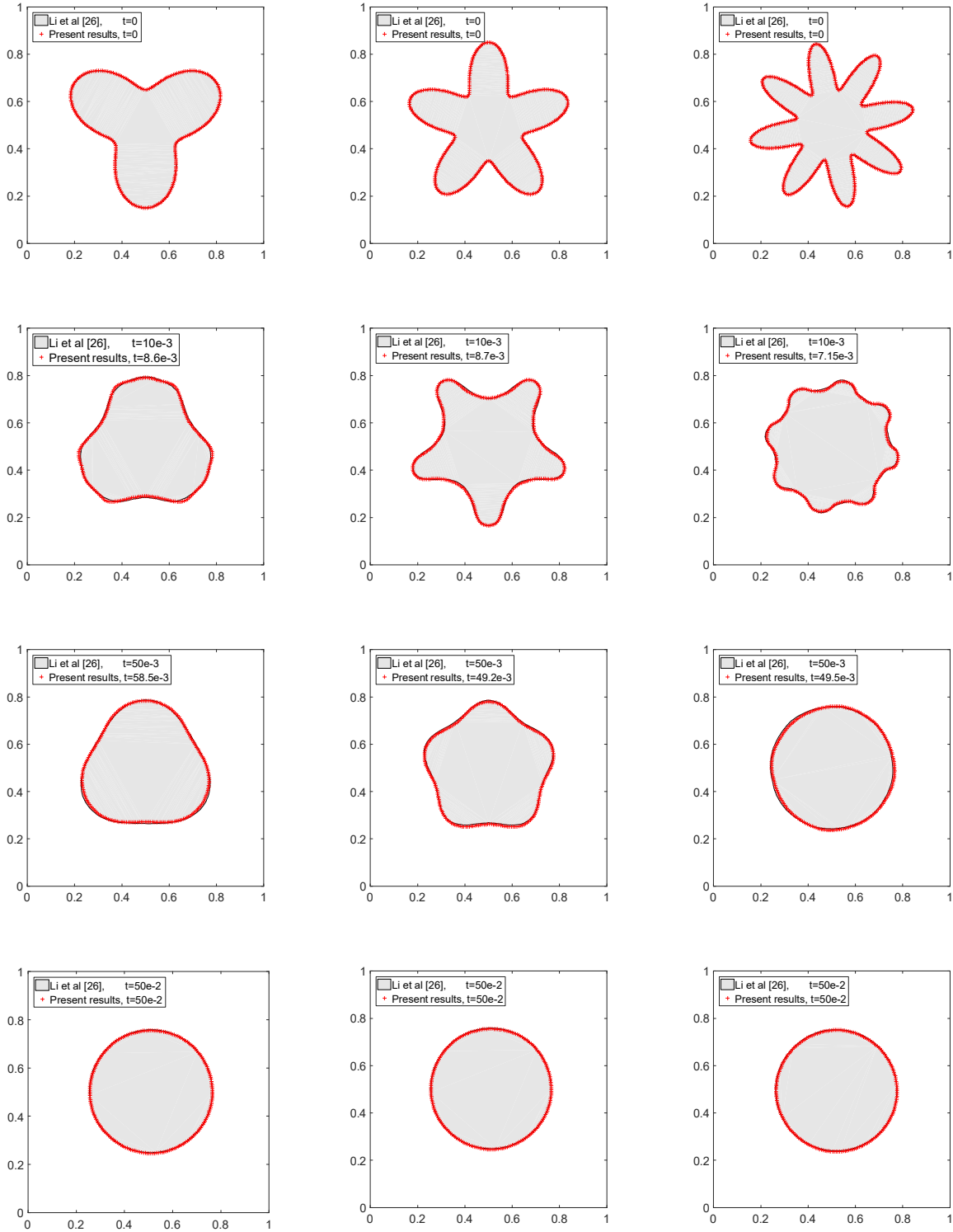


FIG. 3.12. Verification of the time instances of a rosette drop characterized by 3, 5, and 8 modes initial shape when relaxing to circular disc in quiescent liquid.

Despite implicit representation of the surface stress forces, parasitic currents arise with maximum magnitude in the close vicinity of the interface, as shown in Fig. 3.13. A reason for the presence of these currents is a slight imbalance between stresses in the interfacial region. The source of the unbalanced stresses is apparently related to the truncation error associated with the second derivative of the Lagrangian coordinate \mathbf{X} (see Eq. (2.15)) when calculating the local surface tension force. Nevertheless, the maximal magnitude of the parasitic velocity does not exceed 0.6% of the characteristic velocity \mathbf{U} , which is too small to have any effect on the transient and steady-state dynamics of the flow under consideration.

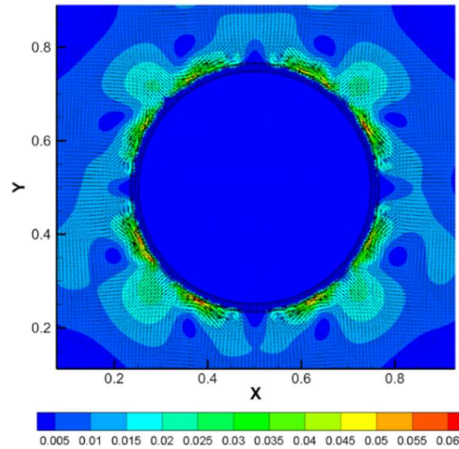


FIG. 3.13. The magnitude of parasitic velocities observed for a drop of circular disc shape.

3.5 Additional capabilities of the algorithm

In this section, we examine additional capabilities of the algorithm to demonstrate that the developed methodology can favorably address both shear and buoyancy-driven flows in which multiple break-up phenomena take place. We first simulate a multiple break-up phenomenon for the flow configuration consisting of a circular drop under the action of pure shear flow. The drop is placed in the center of a long 10×1 channel with no-slip velocities $U\hat{i}$ and $-U\hat{i}$ at the top and the bottom walls, respectively, and periodic boundary conditions

in the horizontal direction. Gravity is neglected. The values of the physical parameters used in the simulation are given in Table 9.

Table 9. The values of physical properties and operating conditions used for 10:1 pure shear flow.

| Re | We | Fr | ρ_1 / ρ_2 | μ_1 / μ_2 |
|------|------|------|-------------------|-----------------|
| 1 | 7.2 | 1 | 1 | 1 |

The time evolution of the drop shape is shown in Fig. 3.14. At times $70 \leq t \leq 100$ the obtained results qualitatively repeat the instability phenomena observed at the central portion of the bubble [75]². The instability is preceded by elongation of the drop, which resembles the shape of a dumbbell at $t = 40$, and is then followed by a detachment of daughter drops via an end-pinching mechanism at $40 \leq t \leq 70$. It is remarkable that while spreading over the channel, the slopes of the elongated drop and a series of its daughter drops further created as a result of the drop break-up asymptotically decrease to approximately zero.

² The values of Re and We were multiplied by a factor of 8 to fit the scaling of the present study.

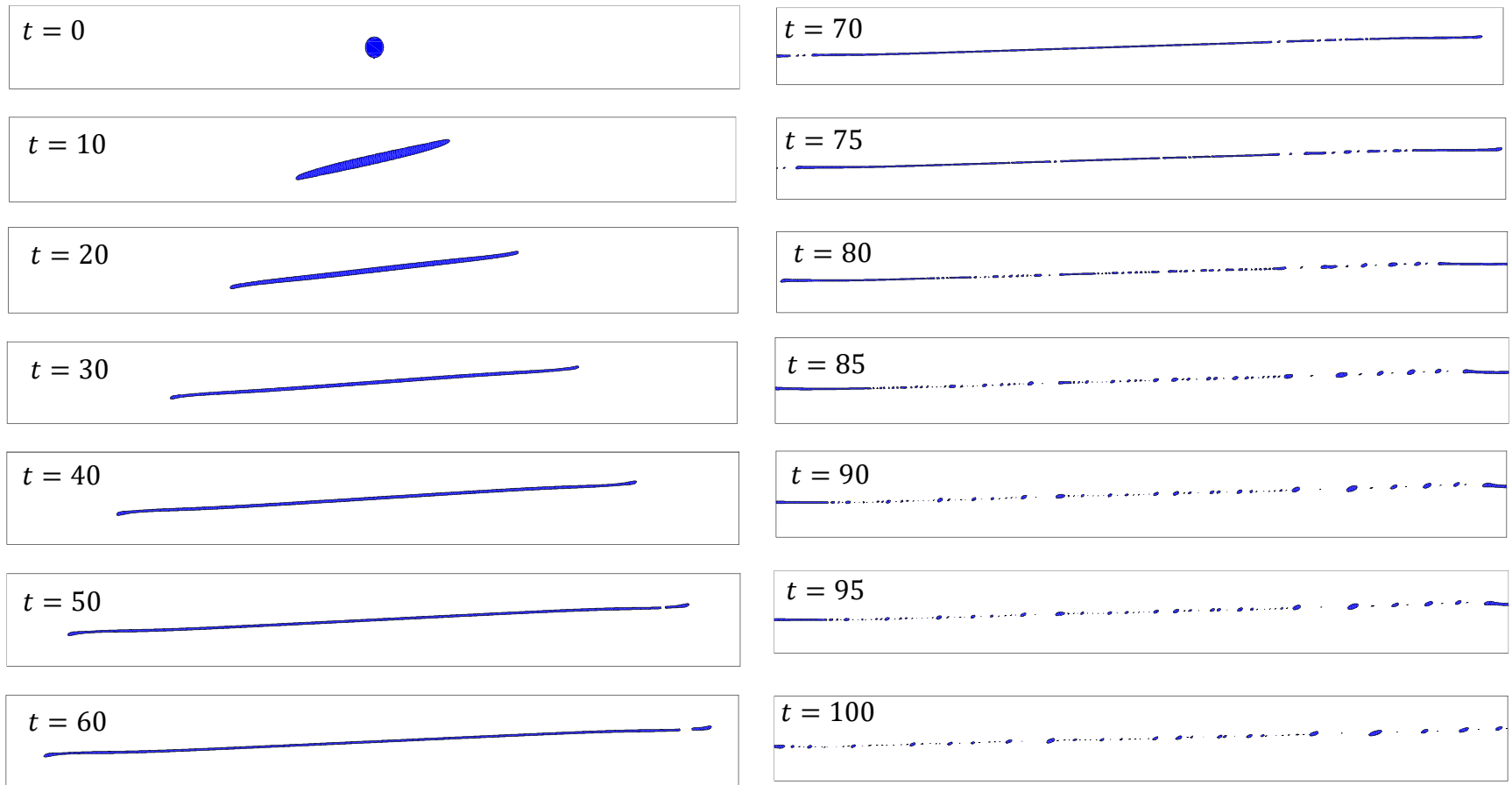


FIG. 3.14. Interface evolution of circular drop under pure shear flow undergoing multiple break-up phenomena, $Re = 1$, $We = 7.2$, 10×1 channel, on a 50×500 grid.

We next simulate a multiple break-up phenomenon by analyzing the configuration corresponding to the rising air bubble in water. The simulation was performed for the physical parameters listed in Table 10. Density and dynamic viscosity ratios were chosen to fit the air-water two-phase flow. The relatively high value of the We number was taken to diminish the surface tension effects and to ensure that the break-up phenomenon takes place before the bubble reaches its terminal velocity.

Table 10. The values of physical properties and operating conditions utilized for the configuration corresponding to the air bubble rising in water.

| Re | We | Fr | ρ_1 / ρ_2 | μ_1 / μ_2 |
|------|------|------|-------------------|-----------------|
| 300 | 2.6 | 1 | 1000 | 185 |

The time evolution of a rising bubble for a number of time instances $t=0.5, 1, 1.5, 2, 2.5, 3$ is presented in Fig. 3.15. At the beginning of the motion, the bubble undergoes deformation stages similar to those observed for test case 2. The crescent shape of the air bubble at $t = 0.5$ is transformed to the shape of a dumbbell, followed by further twisting and thinning at its ends and finally leading to flow instability and the multiple break-up phenomenon at $t = 3$.

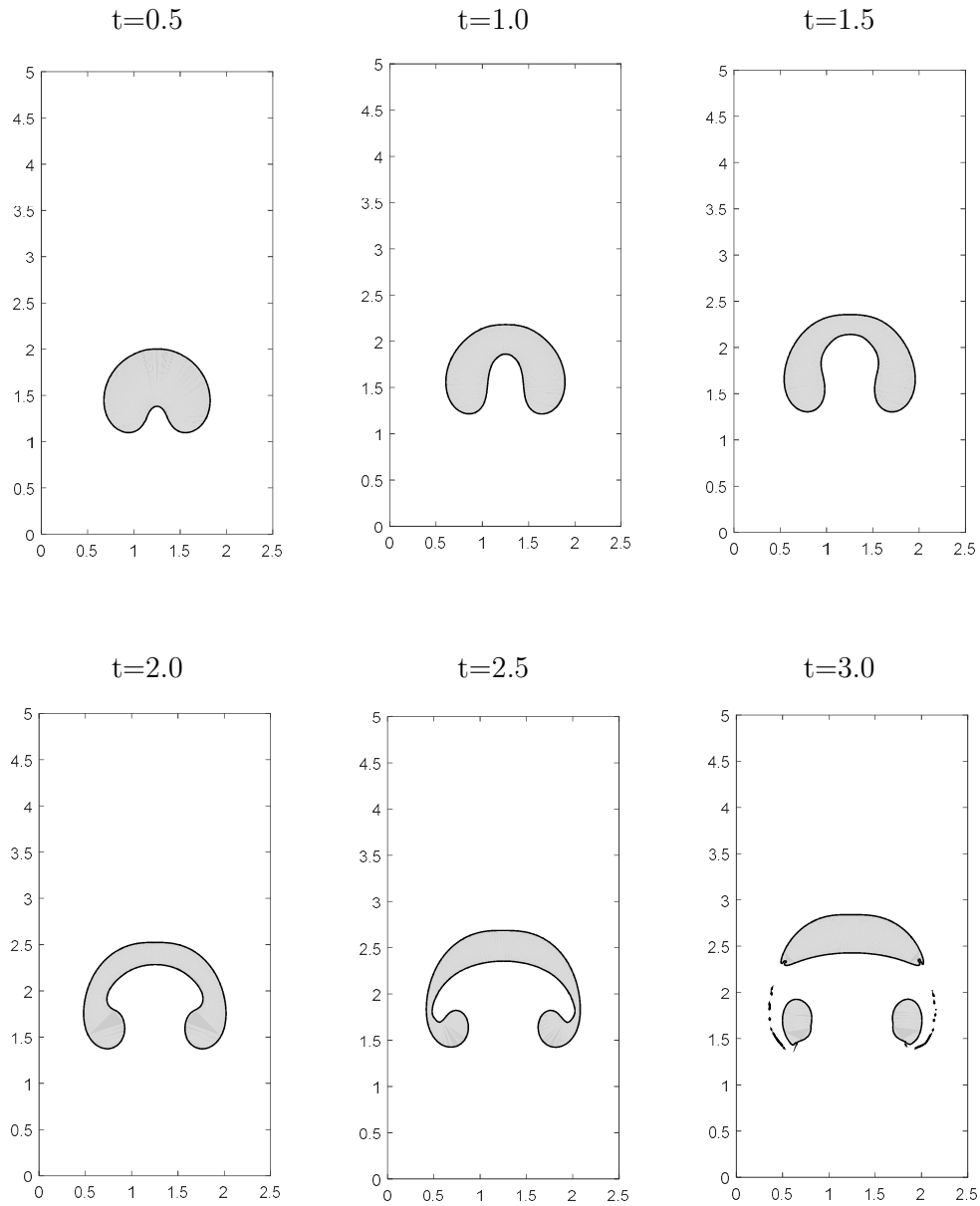


FIG. 3.15. Interface evolution of circular air bubble rising in water. The simulations were obtained for $Re = 300$, $We = 2.6$, $Fr = 1$ on a 320×640 grid.

3.6 Test case 5 – Fiber optic coupler

In the current study we aim to demonstrate the capabilities of the developed numerical tool in order to simulate fusion dynamics of optic fiber couplers to further facilitate their fabrication. We start with a comparison of the currently obtained numerical results with the corresponding numerical and experimental data obtained by Pone et al. [1] for the fusion of two SMF28 fibers of $125 \mu\text{m}$

diameter, as shown in Fig. 3.16. The fibers were brought into contact and heated with a propane micro-torch at a temperature of about 1400 °C.

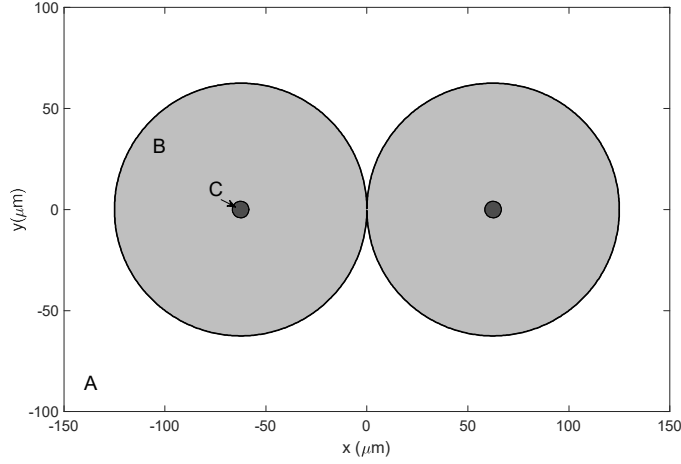


FIG. 3.16. Initial configuration of two SMF28 fibers: A, B, and C represent air, the fused silica fibers, and the concentration of dopants, respectively.

A structure identical to the one tested in ref. [1] was simulated by plugging in the same environmental and material conditions and setting the pulling speed v_s to zero. The degree of fusion and the external shape of the fused fibers were then deduced and compared.

The numerical simulations were performed on a $400 \times 600 \mu\text{m}$ domain to minimize the impact of the boundaries. The physical properties that were used in the numerical simulations are given in Table 11.

Table 11. Physical properties of fused silica and air used for the validation procedure.

| | $\rho[\text{kg}/\text{m}^3]$ | $\mu[\text{Pa}\cdot\text{s}]$ | $D[\text{m}^2/\text{s}]$ | $\sigma[\text{N}/\text{m}]$ |
|--------------|------------------------------|---------------------------------|--------------------------|-----------------------------|
| Fused silica | 2200 | 1.15×10^5 ^a | 1.51×10^{-14} | 0.272 ^a |
| Air | 0.185 | 6.01×10^{-5} | | |

^a Viscosity and surface tension coefficients of the fused silica were adopted from ref. [1].

A comparison between the results obtained in the current work and those published in ref. [1] is given in Fig. 3.17. The results depicted in Fig. 3.17 do indeed show good agreement between the current simulation and the measurements and numerical results presented in [1]. Nonetheless, validation of

the numerical method is still needed for more complex situations involving asymmetric structures, internal dopant flow, diffusion and pulling, as will be discussed in subsequent sections.

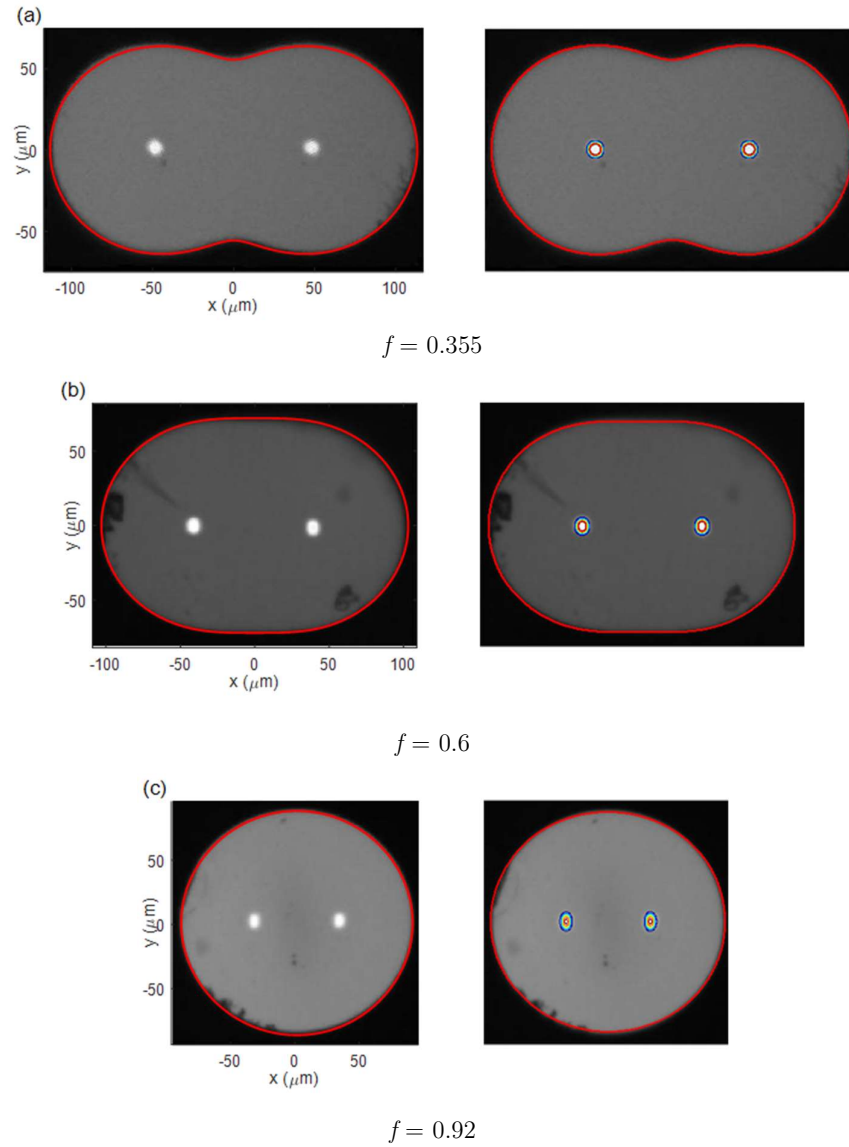


FIG. 3.17. Comparison of the simulation results (solid red line) obtained in the current work (left) to the results of Poné et al. [1] (right). The cross-sections are at: (a) $f = 0.355$, (b) $f = 0.6$, and (c) $f = 0.92$.

Chapter 4: Experimental setup

The primary purpose of the experiments reported here was to test and validate the numerical methodology in complex situations and to study its accuracy and limitations. For this purpose, several fused fiber components were fabricated and analyzed. To fabricate the components, a commercial scanning hydrogen flame glass-processing workstation (Lighted CW-5000) was used. In all the test cases except for one (in which a non-circular fiber was tested), two optical fibers were stripped, cleaned, and fixed in a holder, ensuring good physical contact between them (see Fig. 4.1). The fibers were then slowly pulled, while the scanning hydrogen flame provided the energy required to transform the glass into an effective viscous fluid. Scanning the flame back and forth along a preset length of the contacting fibers at a much higher rate than the pulling rate provided a zone of an effective constant temperature [76], quantitative justification for this assumption is given in appendix I. The flame was set to scan a total length of 10mm at a rate of $500 \mu\text{m/s}$. The pulling rate was set to $0.75 \mu\text{m/s}$. The process was terminated after about two hours when the pulled length had reached 10 mm. The temperature of the glass was approximated to be 1650°C .

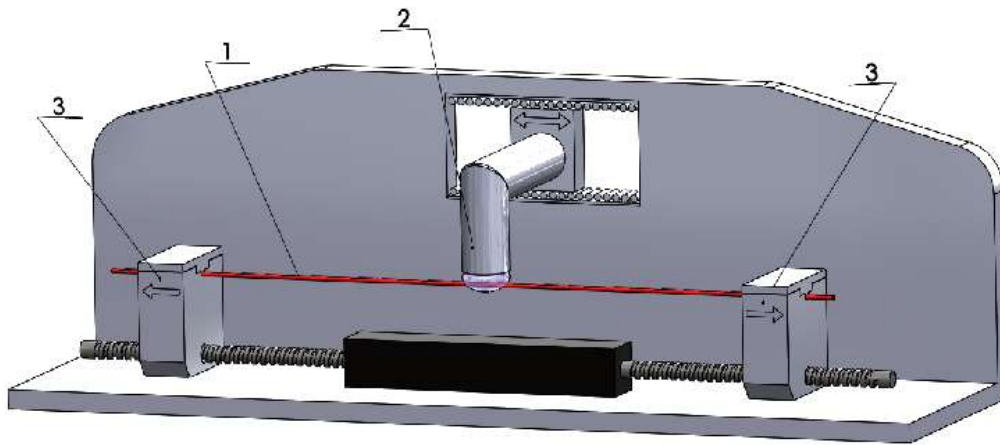
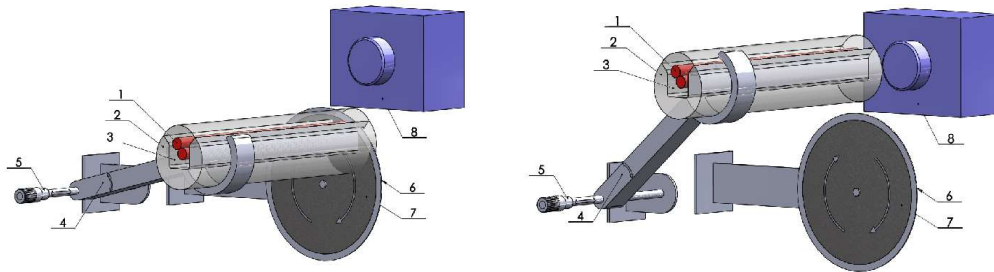


FIG. 4.1 Illustration of the glass processing workstation. The main components are: 1 - optical fibers, 2 - scanning flame, 3 - pulling holders.

At the end of each fabrication process, the new optic fiber component was inserted into a U-shaped glass ferrule. The ferrule was filled with epoxy resin and subjected to UV curing to form a rigid material encapsulating the fiber

component, which was then placed in a holder positioned in a micrometer screw. Next, the end of the ferrule with its epoxy-immobilized fiber component was sliced off (using a turning diamond disc), and the cut end was polished (with a polishing sheet), as depicted in Fig. 4.2. The polished end was then examined under a microscope, and its cross-sectional shape was recorded with a camera. The process was repeated a number of times. Combining the photographs of the fused component along its longitudinal axis enabled a 3D reconstruction of its shape. To minimize the uncertainty as to the location of each cross-sectional measurement, slicing, polishing, and recording was performed using the same fixture. Nevertheless, there are a number of uncertainties inherent to the experimental setup. A full description of the uncertainties and their consequences to the experimental results is given in appendix II.



(a) The first step of measurements. The coupler was sliced and polished at a precise cross-section.

(b) The second step of measurements. The coupler's cross-section was photographed.

FIG. 4.2. The measurement setup: 1 - fused coupler, 2- U-shaped glass, 3- epoxy resin, 4- holder, 5- micrometer screw, 6- edge of the rotating cutting disk, 7- rotating sandpaper, 8- camera.

To cover the wide spectrum of the parameters, the simulations and experimental analyses were performed and compared for four different types of components (see Fig. 4.3). The first most basic component (coupler) was prepared from two SMF-28 single-mode fibers (125/8.2 μm cladding/core diameters) and was used for examining the fully symmetric configuration. The second type was composed of an SMF-28 fiber combined with a 125/106 μm diameter (cladding/core) fiber. In this case – referred to as the pump-SMF coupler later in the thesis – the external interface of the coupler was symmetric, and the core-refractive index of the fibers was not symmetric. The large core of the 125/106 μm fiber facilitated the tracking of the core interface. The third type of coupler constituted a fully non-symmetric configuration produced from two fibers, one

with a $125\ \mu\text{m}$ outer cladding diameter and the other with a $80.3\ \mu\text{m}$ outer cladding diameter. The fourth configuration had the most complex geometry—that of non-circular fiber tapering. Our working hypothesis for this study was that once the developed numerical methodology had been validated for accurate prediction of the characteristics typical of the four above configurations, it could also be used for the theoretical analysis of optical fibers having a wide variety of external shapes (other than those used here) and internal compositions.

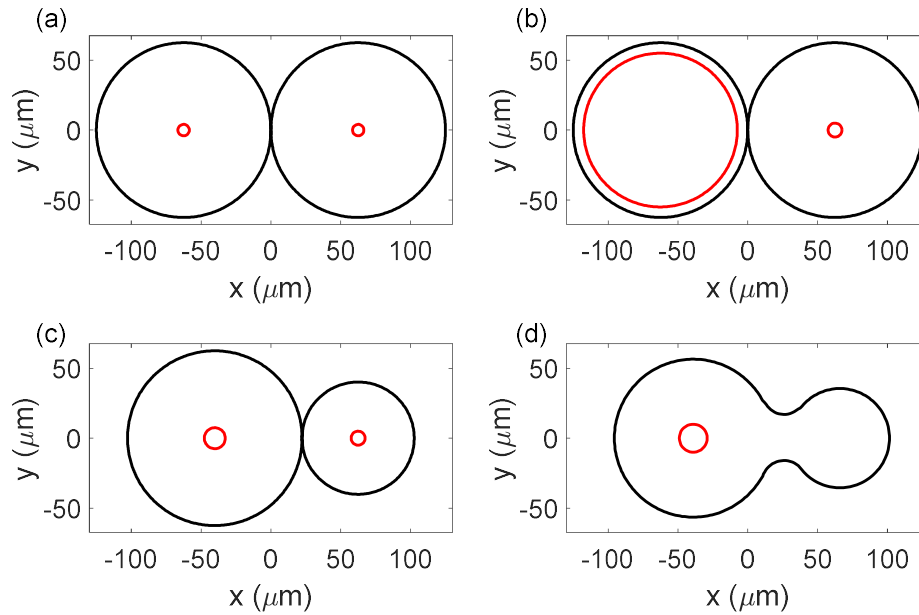


FIG. 4.3. Initial configurations of the analyzed cases, where the black lines represent the external interface, and the red line shows the shape of the initial core: (a) fully symmetric case, (b) symmetry only of the external interface, (c) non-symmetric case, and (d) complex geometry.

Chapter 5: Calibration and similarity analysis

Prior to describing the series of numerical simulations and experiments that were conducted, we point out two major factors that can result in significant deviations between the numerical and the experimental results. The first factor is the strong dependence of the viscosity of fused silica on the temperature [77, 78]. This is in contrast to the density ($\sim 2200 \text{ kg/m}^3$) and the surface tension coefficient ($\sim 0.3 \text{ N/m}$) of fused silica, known to be only slightly dependent on temperature variations [77]. To illustrate this factor, we present the time evolution of the degree of fusion, f , calculated for several values of the viscosity of the fused silica, as shown in Fig. 5.1. The time evolution was calculated for viscosity values lying in the range of $\mu = (5\text{--}50 \text{ GPa}\cdot\text{s})$, which corresponds to the typical range of working temperatures $T = (1800\text{--}1650 \text{ }^\circ\text{C})$, respectively. As can be seen from Fig. 5.1, the f values measured at the same time instance can deviate by up to five-fold, which stresses the need for careful calibration of the viscosity of the fused silica as a function of temperature. The second factor stems from a strong dependency of the viscosity of fused silica on the absorption rate of hydroxides (OH) formed on the fiber surface during heating by the hydrogen flame [79]. This dependency can result in a significant deviation between the numerical and experimental results for long-term heating processes.

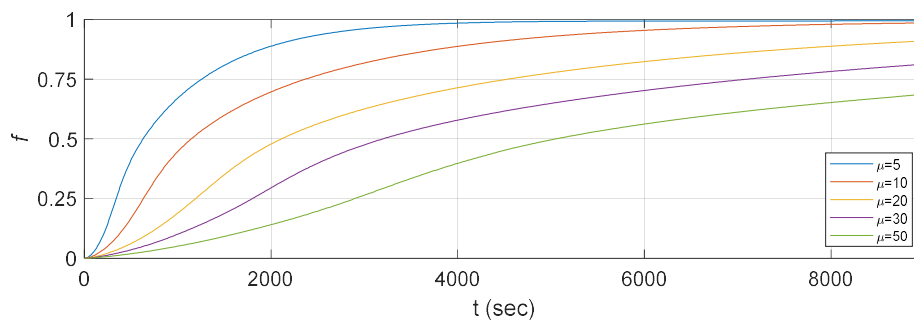


FIG. 5.1. Time evolution of the degree of fusion for several values of the viscosity. ($v_s = 0$)

Since it is difficult to calculate and measure the OH concentration during the fabrication process, the time dependence of the fused silica fibers subjected to a constant hydrogen flame at a constant temperature was approximated by the following relation:

$$\mu(t) = (\mu_0 - \mu_s)e^{-\lambda t} + \mu_s, \quad (5.1)$$

where μ_0 , μ_s , and λ are the initial viscosity, the viscosity at the saturated state, and the OH absorption rate, respectively [79].

Significant variation of the viscosity values and the marked impact of this variation on the degree of fusion motivated us to perform a similarity analysis that would allow us to cancel out the dependence of the degree of fusion on the viscosity of the fused silica. The similarity was achieved by representing the degree of fusion as a function of the aspect ratio, H / W of the coupler, as defined in Fig. 5.2. As a result, the simulated degree of fusion was correlated with the aspect ratio of the coupler, regardless of the viscosity values (see Fig. 5.3).

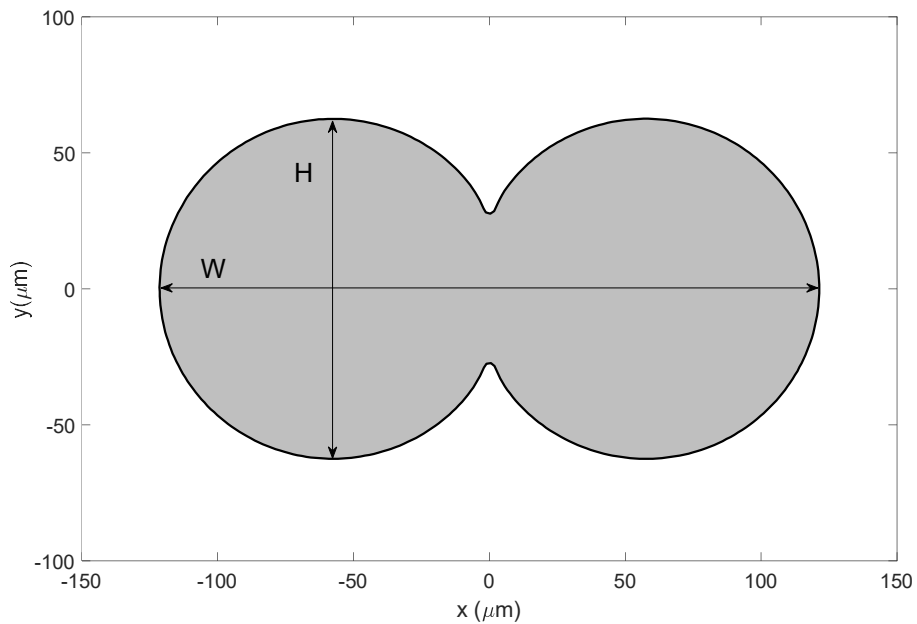


FIG. 5.2. Geometric dimensions of a typical coupler.

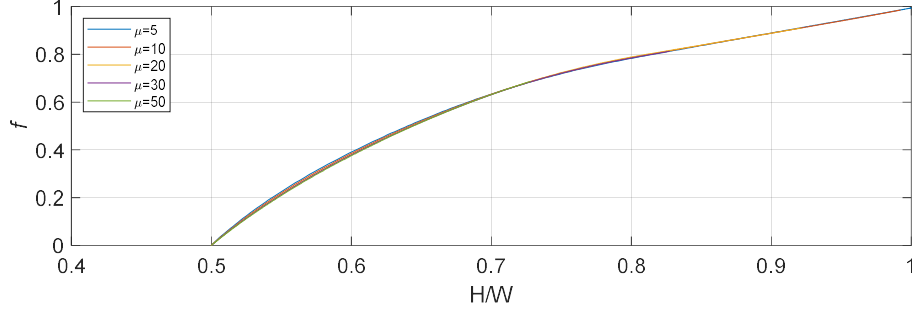


FIG.5.3. Evolution of the degree of fusion for several viscosity values as a function of the aspect ratio H/W of the coupler ($\nu_s=0$).

In addition, to characterize the evolution of viscosity in the current experiments, the problem was simulated with several initial and saturated viscosities and different OH absorption rates. It was found that the values of $\mu_0 = 50 \text{ GPa}\cdot\text{s}$, $\mu_s = 5 \text{ GPa}\cdot\text{s}$, and $\lambda = 6 \cdot 10^{-4} \text{ s}^{-1}$ provide the best correlation with the experimental results.

In contrast to the degree of fusion determined by Eq. (1.2), the pulling rate was not equal to zero in the current experiments and simulations, and therefore W_0 and W_∞ were not constant during the process and had to be evaluated at each time instance for each cross-section. The relationship between W and the cross-sectional area is given by $[W_0(t), W_\infty(t)] \propto \sqrt{A(t)}$ and hence the modified fusion degree (MFD) is expressed by:

$$f_m = \frac{W_0(t) - W(t)}{W_0(t) - W_\infty(t)}, \quad (5.2)$$

Where $W_0(t) = \frac{W_0(0)}{\sqrt{A_0}} \sqrt{A(t)}$ and $W_\infty(t) = \frac{2}{\sqrt{\pi}} \sqrt{A(t)}$. In the current experiments,

the area $A(t)$ and the width $W(t)$ were measured to evaluate the MFD for each cross-section, and the height $H(t)$ was measured to calculate the aspect ratio of the coupler ($H(t) / W(t)$).

Chapter 6: Results

In this chapter, the numerical simulation and experimental results are presented and compared. The experimental results were obtained by the methodology described in chapter 4. The numerical simulations were performed for initial structures, as shown in Fig. 4.3, while the dynamic properties (density, viscosity, and surface tension coefficient) were taken from the literature [77, 78] and have been further fine-tuned by adapting them to the currently acquired experimental results, as described in the previous chapter. For the sake of completeness, we will also introduce the dynamic properties here: the density and the surface tension coefficient of silica are approximately equal to $\sim 2200 \text{ kg/m}^3$ and $\sim 0.3 \text{ N/m}$ [77, 78], respectively. The viscosity of the silica in the initial and the saturated state for different OH absorption rates were evaluated to be $\mu_0 = 50 \text{ GPa s}$, $\mu_s = 5 \text{ GPa s}$, and $\lambda = 6 \cdot 10^{-4} \text{ s}^{-1}$ [see Eq.(5.1)].

Table 12 - The values of dynamic properties and experimental operating conditions.

| ρ_x | μ_0 | μ_s | λ | σ | \bar{D} | l | v_s | Δt |
|-----------------|----------------|----------------|-----------------|--------------|-----------------|-------------|-----------------|------------|
| kg/m^3 | GPa s | GPa s | s^{-1} | N/m | $\mu\text{m/s}$ | nm | $\mu\text{m/s}$ | s |
| 2200 | 50 | 5 | 6E-4 | 0.3 | 2.72E-2 | 10 | 0.75 | 10 |

All the numerical simulations were performed for a computational domain of $600\mu\text{m} \times 400\mu\text{m}$, while the grid resolution was 675×450 . The boundary conditions utilized in the numerical simulations were the Dirichlet boundary condition for pressure and a zero gradient value for all the velocity components at all four edges of the computational domain. The initial values of the concentration in the numerical simulations were set to unity, representing the normalized value related to the initial concentration. The experimental analysis and the simulation results are presented and discussed in the following sections.

A number of representative simulations were also performed on a 1350×900 grid in the framework of a grid independence study. It was found that the discrepancy between the degrees of fusion obtained on the two grids did not

exceed 3%, thus allowing us to perform all the simulations on the 675×450 grid. Remarkably, the maximal discrepancy between the results obtained on the two grids was observed at the beginning of the numerical simulations, as a result of exceptionally high values of the interface curvature at the point of contact between the two fibers. The dimensional computational time step used in all the simulations was equal to 10 s, which is sufficient when taking into account that the duration of a typical production process in the conducted experiments was more than two hours. For shorter durations of the production process, smaller values of the computational time step should be used.

The initial values of the concentration in the numerical simulations were set to unity, representing the normalized value related to the initial concentration. The experimental analysis, as well as simulation results, are presented and discussed in the next section.

6.1. The numerical simulations and the experimental results

6.1.1. Symmetric two-SMF coupler

A qualitative comparison between the experimentally and numerically obtained external shapes of the coupler and the spatio-temporal distribution of the dopant within the coupler's core - determining the refractive index profile (under the assumption of linear dependence of the dopant concentration on the refractive index) is given in Fig. 6.1. Each row is related to a specific cross-section of the coupler, corresponding to a given time instance. The first and the third columns represent the experimental and the numerical results, respectively, while the second column represents a superposition of the two. The fourth column is a close-up of the core area of the left fiber.

As shown in Fig. 6.1, good correlation was found between the experimentally and numerically obtained external boundaries of the coupler for the entire range of time instances. Additionally, an acceptable qualitative agreement between the distribution of the dopants in the core of each fiber allowed reliable prediction of their spatio-temporal concentration distribution and

the refractive index profile. Note that the glare areas clearly visible on the photographs acquired in the course of experiments were generated by an external light source. As such, the areas constitute only qualitative characteristics of the spatial distribution of the dopants. Nonetheless, the numerical results predict a significant (between 4- and 10-fold) decay of the peak concentration values with time (see the fourth column in Fig. 6.1).

A quantitative comparison between the numerically and experimentally obtained evolution areas and the MFD [see Eq.(5.2)] is given in Fig. 6.2. It can be seen from the figure that the numerically obtained temporal evolutions of the area and the MFD are cross-correlated with the corresponding experimentally measured values for the entire range of time instances, which successfully validates the developed quasi-3D model. We note in passing that at the beginning of the numerical simulations values of the MFD are very small ($0(10^{-3})$), but still negative values of the MFD were obtained. This unphysical result may be attributed to the numerical error resulting from exceptionally high values of the interface curvature and could be corrected by applying simple filtering, replacing the negative unphysical values by zero.

We next present the numerically and experimentally obtained results correlating the MFD with the height-to-width ratio of the coupler, as shown in Fig. 6.3. Good agreement between the numerical and experimental results was obtained. Note that the results shown in Fig. 6.3 are invariant to the viscosity values. The presented MFD height-width ratio relationship directly affects the overall fusion time and indirectly affects the distribution of the core dopants. The graph in Fig. 6.3 may assist coupler design by serving as a preliminary tool for estimating the MFD from the external dimensions of the fibers

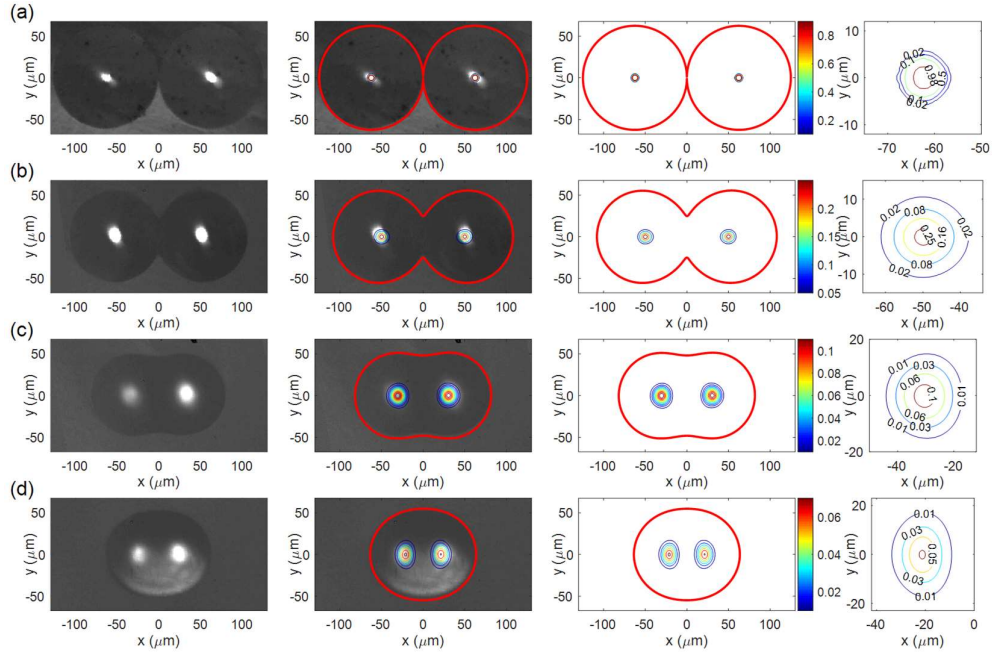


FIG. 6.1. Experimentally and numerically obtained cross-sections of a fully symmetric SMF fiber coupler at different time instances: (a) 30 s, (b) 1650 s, (c) 3600 s, and (d) 5300 s. Columns 1 and 3 show the experimental and simulation results, respectively; column 2 shows a superposition of columns 1 and 3, and column 4 shows close-ups of the numerically predicted core area of the left fiber.

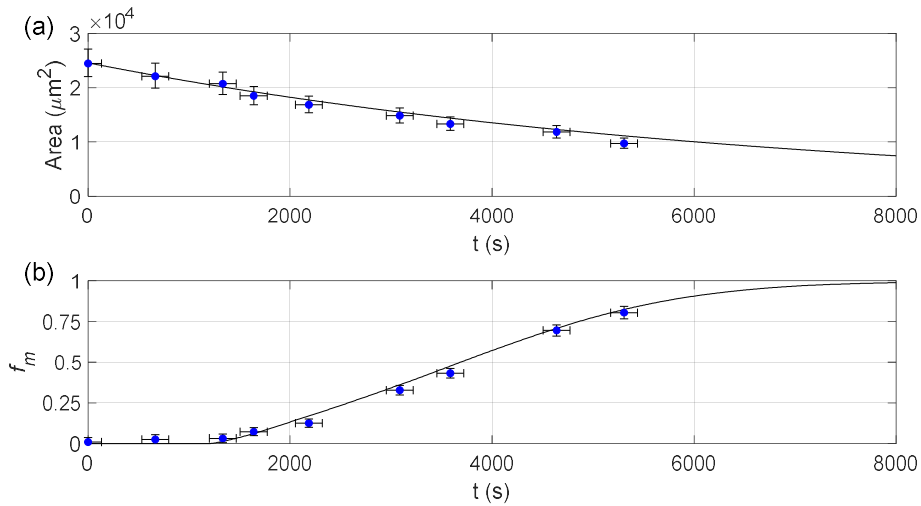


FIG. 6.2. Comparison between the numerically and experimentally obtained temporal evolutions of the cross-sectional area and the MFD typical of the symmetric coupler. Line – Simulation results, Points – Experimental results. (a) The decrease in area with time. (b) Temporal evolution of the MFD.

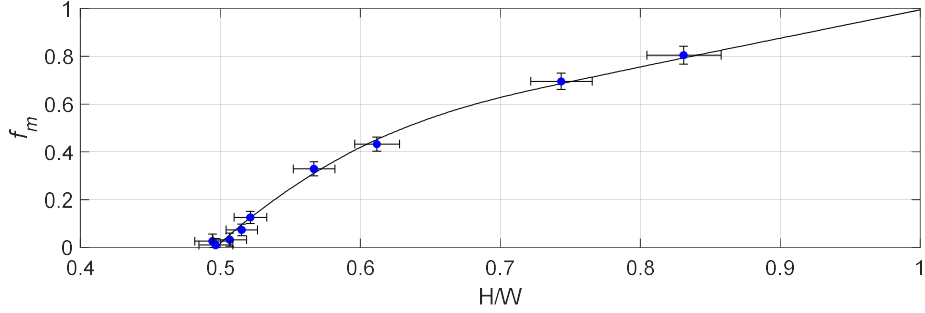


FIG. 6.3. Comparison between the numerically and experimentally obtained temporal evolutions of the MFD as a function of the coupler dimensions. Line – Simulation results, Points – Experimental results.

6.1.2. Pump-SMF coupler

The pump-SMF coupler configuration is characterized by a symmetric external shape, while the core of one of the fibers is much bigger than the core of its counterpart. This setup allows for more efficient tracking of the experimentally acquired data regarding the spatio-temporal distribution of the dopants in the cores. A comparison between the simulation and the experimental results acquired at four different time instances revealed an acceptable agreement between the numerically and experimentally obtained characteristics of the coupler for the entire range of time instances (Fig. 6.4). In contrast to the simple configuration, the core of the left fiber intersects the vertical centerline crossing the domain at $x = 0$ in the course of the fusion process (see Fig. 6.4 (d)). Note that from a numerical point of view, the observed spatial expansion of the core of the left fiber was attributed to the molecular diffusion resulting from one-way coupling between the NS [Eq.(2.5)] and convection-diffusion [Eq. (2.6)] equations. The assumption of one-way coupling adopted in the current study was validated by the good qualitative agreement obtained between the experimentally and numerically obtained spatio-temporal distributions of the dopants in the coupler core.

The obtained results also successfully verified the correctness of the implementation of the boundary conditions applied to the coupler boundary, that aim to provide zero concentration flux outside of the dopants out of the coupler. Figure 6.5 presents a quantitative comparison between the numerically and experimentally obtained temporal evolutions of the coupler area and the MFD. It

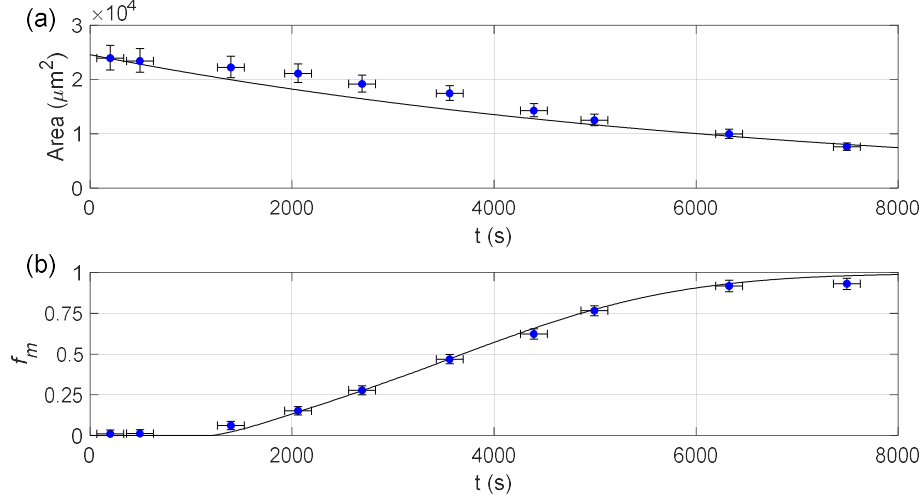


FIG. 6.5. Comparison between the numerically and the experimentally obtained temporal evolutions of the cross-sectional area and the MFD typical of the second test case. Line – Simulation results, Points – Experimental results. (a) The decrease in area with time. (b) Temporal evolution of the MFD.

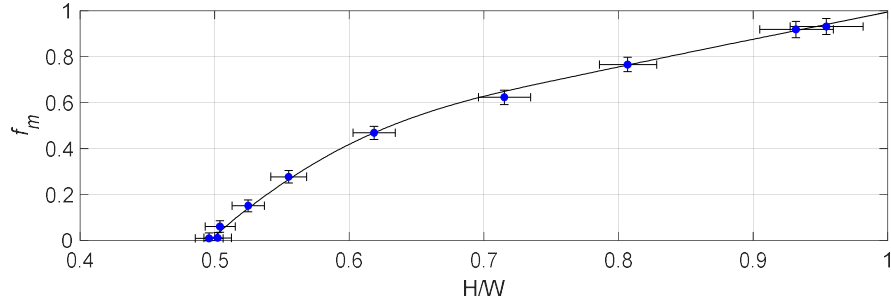


FIG. 6.6. Comparison between the numerically and experimentally obtained temporal evolutions of the MFD as a function of the coupler dimensions for the second test case. Line – Simulation results, Points – Experimental results.

6.1.3. Non-Symmetric coupler

The non-symmetric coupler was prepared by fusing fibers with outer cladding diameters of $125 \mu\text{m}$ and $80 \mu\text{m}$. Comparisons of the experimental and numerical results demonstrated good qualitative agreement for both the outer shape and the spatial distribution of the dopants (see Fig. 6.7) and the temporal evolution of the cross-sectional areas (see Fig. 6.8a). Agreement between the experimentally and numerically obtained time evolutions of the MFD were not as good as that for the areas (see Fig. 6.8a vs. 6.8b): the discrepancies between the values were particularly marked at the beginning and end of the fusion

process, reaching 70% and 10%, respectively. This observation may indicate an overestimation of the viscosity values utilized in the numerical simulations compared to the actual viscosities in the experiments, which resulted in a smoother evolution of the MFD in the numerical simulations. Remarkably, the above notwithstanding, an acceptable agreement was obtained between experimentally and numerically obtained values of the MFD as a function of the coupler cross-section size (see Fig. 6.9). These results indicate that the temporal evolution of the cross-sectional area is primarily determined by the initial geometry of the fibers, while the values of the viscosity and the pulling rate affect the duration of the overall process.

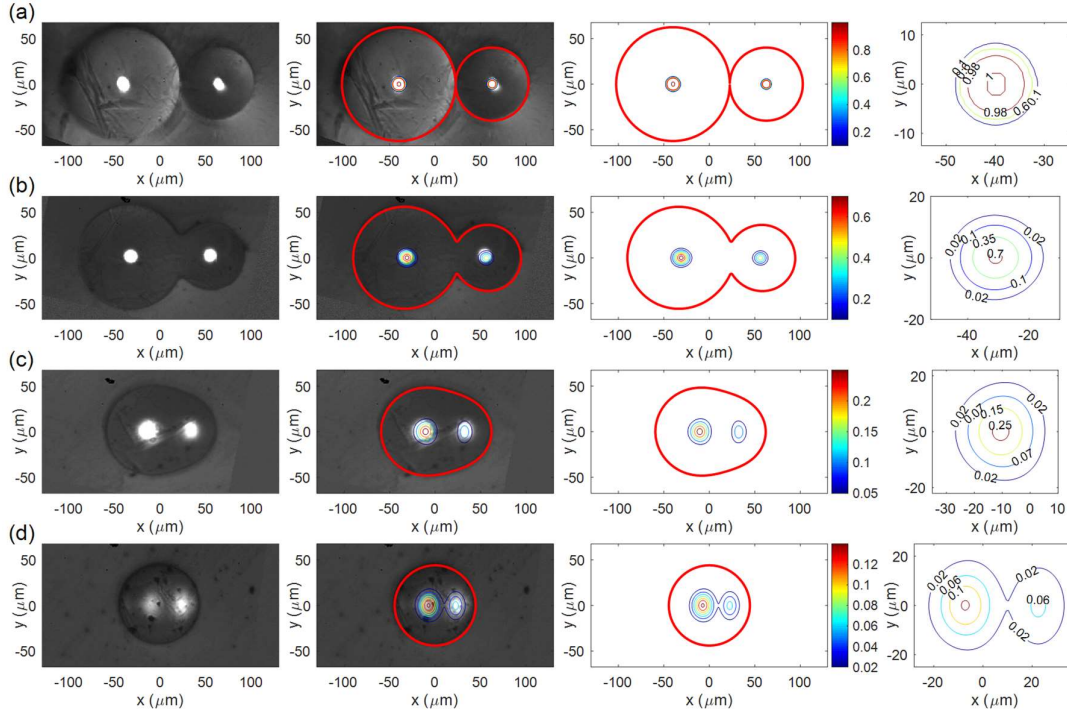


FIG. 6.7. Experimentally and numerically obtained cross-sections of the non-symmetric coupler at different time instances: (a) 30 s, (b) 1350 s, (c) 4300 s, and (d) 7000 s. Columns 1 and 3 show the experimental and simulation results, respectively; column 2 shows a superposition of columns 1 and 3, and column 4 shows close-ups of the numerically predicted core area of the left fiber.

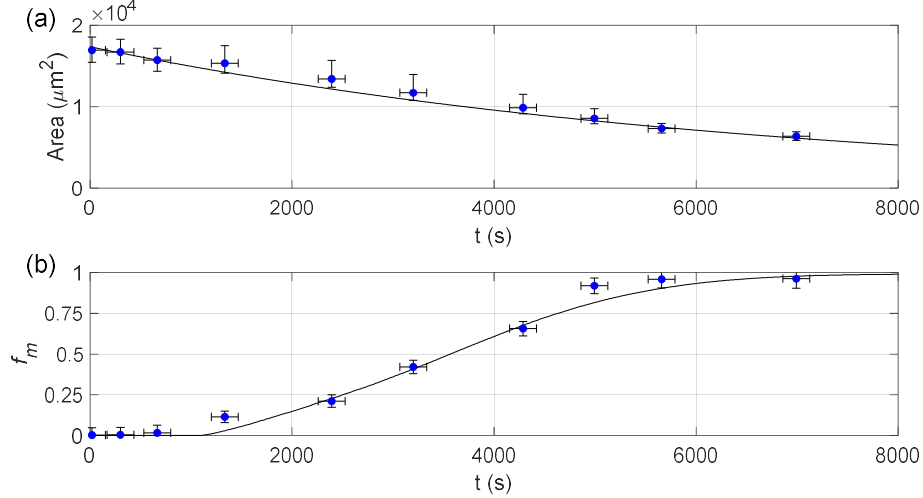


FIG. 6.8. Comparison between the numerically and experimentally obtained temporal evolutions of the cross-sectional area and the MFD typical of the non-symmetric coupler. Line – Simulation results, Points – Experimental results. (a) The decrease in area with time. (b) Temporal evolution of the MFD.

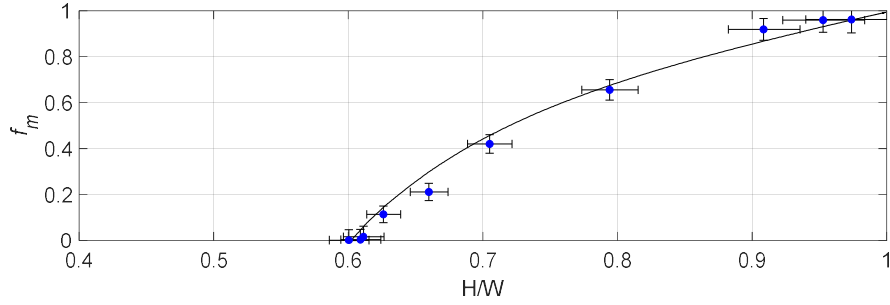


FIG. 6.9. Comparison between the numerically and experimentally obtained temporal evolutions of the MFD as a function of the coupler dimensions for the non-symmetric coupler. Line – Simulation results, Points – Experimental results.

6.1.4. Fiber with a non-circular cross section

The custom-made fiber investigated in this section was characterized by a non-circular cross-section along its entire longitudinal axis (see Fig. 6.10a). In contrast to the previous configurations, the viscosity values at the initial and saturated states were equal to $\mu_0 = 20\text{GPa s}$, $\mu_s = 2\text{GPa s}$, respectively, while the value of the OH absorption rate was equal to $\lambda = 6 \cdot 10^{-4} \text{s}^{-1}$ (the same as that for the previous configurations). Generally speaking, this kind of fiber fulfills its optical purpose in its present form and should not be tapered. Nonetheless, the current test case was processed for the purpose of validation of the developed numerical tool. A comparison between the numerically and experimentally

obtained results revealed good qualitative agreement between the temporal evolutions of the outer shapes of the fiber for all the time instances (see Fig. 6.10). Good agreement for all the time instances was also apparent in a comparison between the numerical and experimental spatio-temporal evolutions of the concentrations of the dopants. Fig. 6.11 shows good correlation between the numerical and experimental results of the cross-sectional area and the MFD time evolutions. Moreover, in this configuration, the time required to obtain full fusion ($f_m = 1$) is much shorter than that for the other test cases, where the viscosity values were higher. Fig. 6.12 also shows the excellent compatibility between the experimentally and numerically obtained values for the temporal evolution of the MFD as a function of the coupler dimensions.

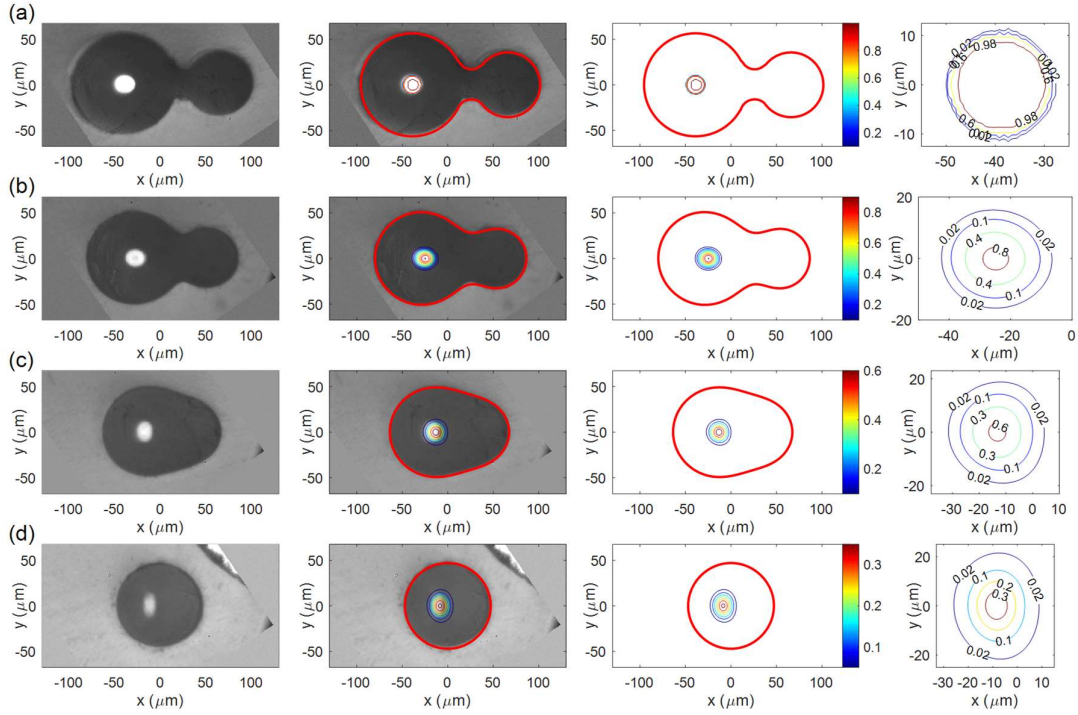


FIG. 6.10. Experimentally and numerically obtained cross-sections of the non-circular tapered fiber coupler at different time instances: (a) 10 s, (b) 1320 s, (c) 2500 s, and (d) 5000 s. Columns 1 and 3 show the experimental and simulation results, respectively; column 2 shows a superposition of columns 1 and 3, and column 4 shows close-ups of the numerically predicted core area of the left fiber.

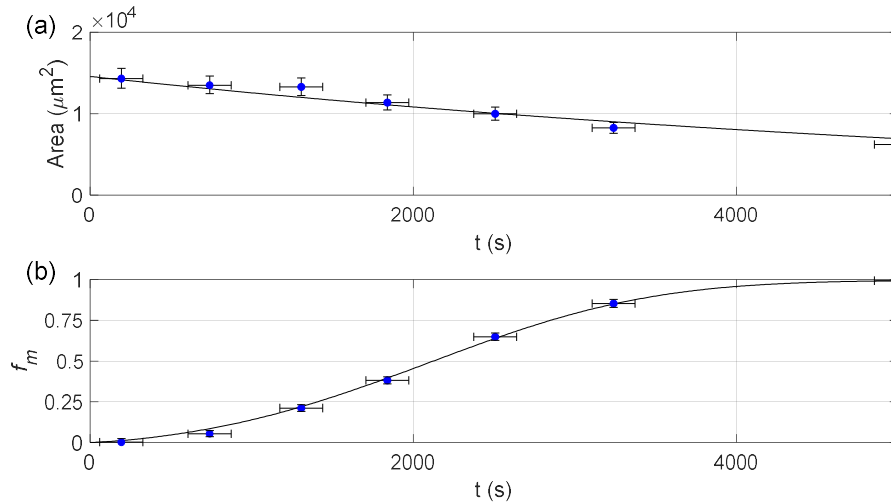


FIG. 6.11. Comparison between the numerically and experimentally obtained temporal evolutions of the cross-sectional area and the MFD typical of a fiber with a non-circular cross section during tapering. Line – Simulation results, Points – Experimental results. (a) The decrease in area with time. (b) Temporal evolution of the MFD.

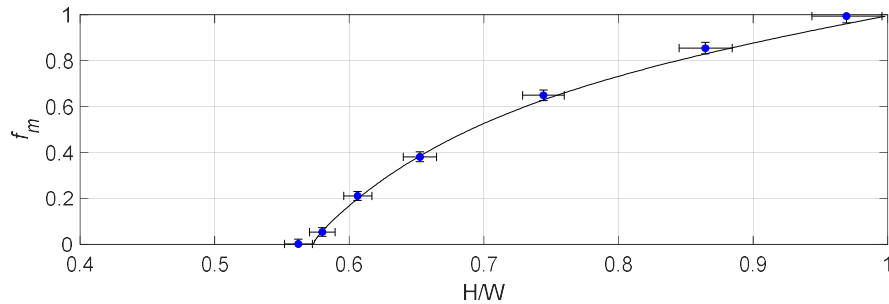


FIG. 6.12. Comparison between the numerically and experimentally obtained temporal evolutions of the MFD as a function of the coupler dimensions for a fiber with a non-circular cross-section. Line – Simulation results, Points – Experimental results.

Fig. 6.13 shows the full 3D shapes of the four types of optical components by superpositioning several cross-sections simulated at a number of consecutive time instances. This kind of data may serve as input for optical numerical simulation packages, such as Opticwave, Rsoft, and Comsol, which can predict the optical performance of the component (such simulations are beyond the scope of this study). Note that the smaller the initial cross-sectional area of the core, the more rapid is the decay of the corresponding concentration peak values of the dopants.

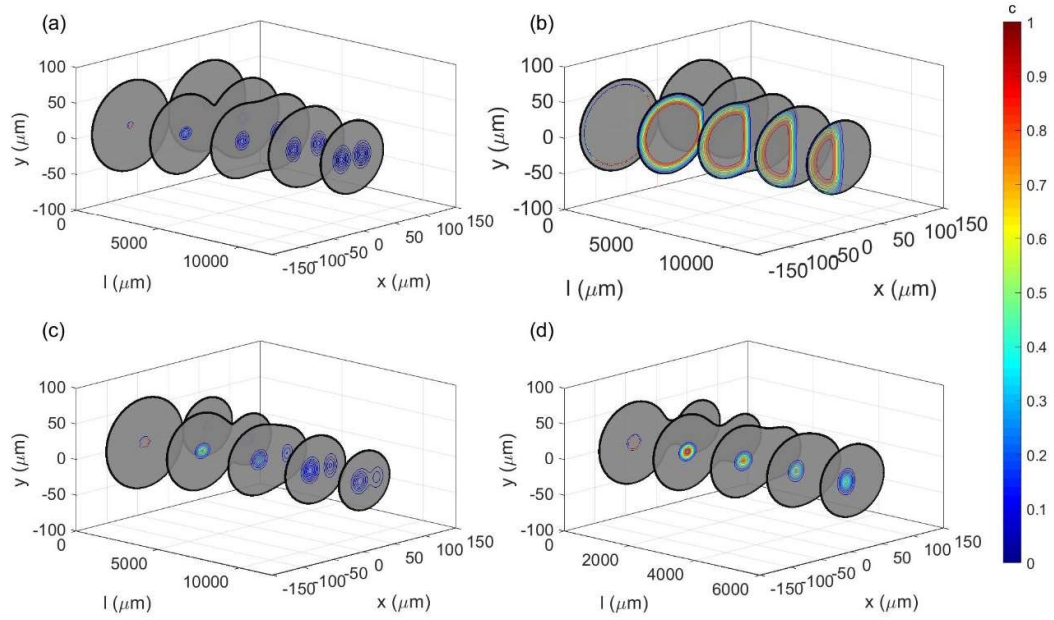


FIG. 6.13. Simulated 3D structure of: (a) a symmetric coupler, (b) a coupler composed of pump (125/106 μm) and SMF (125/8 μm) fibers, (c) a non-symmetric coupler, and (d) a tapered non-circular fiber. Each cross-section was obtained at different time instances.

6.2. Characterization of the non-symmetric couplers

In the course of the simulations, it was found that the viscosity values have a considerable effect on the overall time required to achieve the complete fusion between the fibers and to provide diffusion of the dopants. It was also found that the values of the aspect ratio H/W and the MFD are almost not affected by variations in the viscosity. For this reason, we simulated several configurations of non-symmetric couplers characterized by various H/W aspect ratios. Fig. 6.14 presents seven curves, each related to a different initial value of H/W , starting from the symmetric case characterized by a value of $H/W=0.5$ and ending with the strongly non-symmetric coupler characterized by a value of $H/W=0.8$. As mentioned above, the mapping so obtained can be used as a preliminary tool used for the design of couplers, as it facilitates the evaluation of the MFD by simple measurements. As can be seen from Fig. 6.14, for all the cases, the MFD started from zero and increased up to unity. It may also be seen that a higher initial value of H/W resulted in faster growth of the MFD,

apparently as a consequence of the higher surface tension forces prevailing throughout the fusion process, in turn, as a result of higher curvature values typical of fibers with smaller cross-sections.

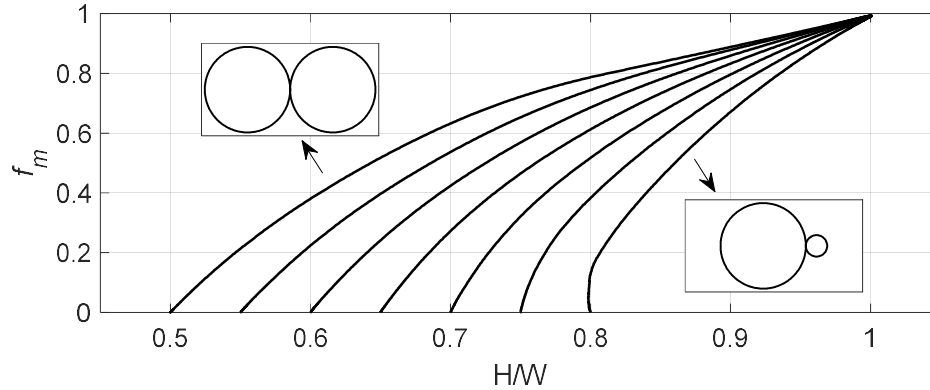


FIG. 6.14. Simulation results of the MFD related to the height-width (H/W) ratio of the coupler for several initial ratios.

6.3. Advanced modeling of multi-fiber combiners

The developed numerical tool can also successfully handle the time evolution of much more complex multi-fiber configurations, incorporating many contact points for each fiber and also including the non-negligible amount of air trapped between the boundaries of adjacent fibers. A representative example of such a simulation is demonstrated in Fig. 6.15, for an optical combiner composed of seven fibers arranged as six fibers circling a central fiber; each fiber touches its neighbor at a single contact point, such that the central fiber has six contact points with all the surrounding fibers, and each external fiber has three contact points with its immediate neighbors. The physical properties of the fiber material are the same as those utilized for the first three configurations (see Chapter 5). In the course of the numerical simulation, the area of air trapped between the boundaries of the neighboring fibers decreases until the total termination of the air regions. The process is simulated explicitly by controlling the air pull-out rate implemented as a distributed sink (Eq. (2.3)) for each air-trapped region. The time evolution of the air-trapped regions and the external interface of the

combiner is governed by the solution of the continuity and NS equations (Eqs. 2.4, 2.5).

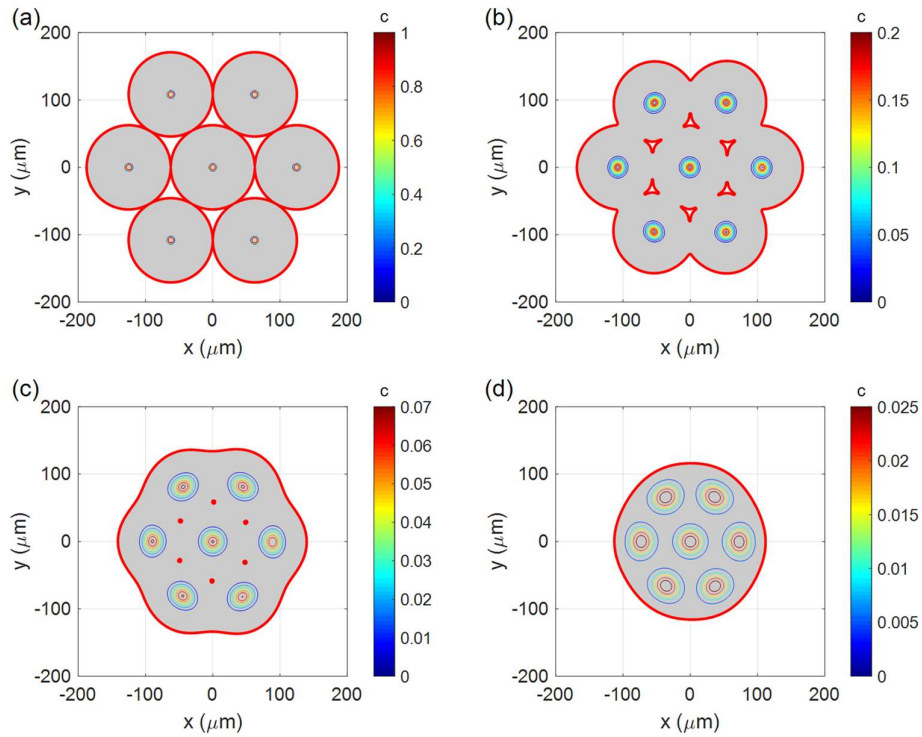


FIG. 6.15. Simulation results for a combiner composed of 7 fibers at times: (a)-Initial state, (b) 900 s, (c) 2500 s, and (d) 5000 s.

It can be seen that in the first stage of the production process, the peripheral fibers evolve non-axisymmetrically (although the periodicity is preserved) due to the initially non-axisymmetric geometry of the air-fiber interface and the air regions trapped between the peripheral and the central fibers. As the tapering progresses, the regions of trapped air are eliminated, and the external shape of the component is smoothed out by the surface tension force, causing the shape of the component to eventually approach a circular configuration. Similar component shapes were obtained experimentally by [80]

Chapter 7: Summary and conclusions

In the framework of the present study, a novel generic numerical methodology was developed for the prediction of the structural features of fiber optical components fabricated by the “heat-and-pull” technique. It was also shown that this methodology can serve to solve a wide range of physical problems involving two-phase flow. The numerical model was based on extending the Immersed Boundary method and the FT approach, as well as on the distributed Lagrange multiplier approach for the configuration of the relevant two-phase immiscible flows. The capabilities of the developed method were demonstrated by utilizing a full pressure–velocity coupled direct solver (FPCD) [50] as a computational platform. The idea underlying the developed approach was that the initial system of fully pressure-velocity coupled continuity and NS equations is extended by including additional relationships implicitly linking the Euler flow fields and the distributed Lagrange multipliers. This linkage enforces kinematic constraints of the impermeability of both fluids on the interface separating the two phases. The fully coupled formulation enables controlling mass conservation (with source) of both phases without the need for any additional correction procedure, which is of significant computational advantage.

The developed method was extensively verified for three typical two-phase flow benchmark cases. In the context of optic fiber components, the quasi-3D approximation was successfully validated by comparing numerical predictions with four different and real optical couplers, representing a wide spectrum of diversity. It was thus demonstrated that the tool could be applied to achieve a reliable spatio-temporal prediction both of the external shape of the fiber components and of the dopants' concentration distribution inside them.

A comparison of the numerical and experimental results also revealed that the viscosity of the fused silica dropped during the fabrication process, despite insignificant temperature variations. This observation may be attributed to the absorption of OH (hydroxyl) in fused silica when the last is exposed to a hydrogen

flame. It is thus essential that the change in the viscosity of the fused silica due to OH absorption will be considered when a hydrogen flame is used to fabricate fused optical components.

The numerical characterization of the structural evolution of couplers was also performed for several non-symmetrical cases, showing that it is possible to evaluate the degree of fusion of a given optical coupler by only measuring its height and width. Finally, a numerical simulation predicting the spatio-temporal evolution of a fused seven-fiber-combiner was presented. This simulation showed that the numerical tool can handle complex geometries and may be used to develop a wide range of fused optic fiber components.

8. References

- [1] E. Pone, X. Daxhelet and S. Lacroix, "Refractive index profile of fused-fiber couplers cross-section," *Optics express*, vol. 12.6, pp. 1036-1044, 2004.
- [2] D. Noordegraaf, P. M. Skovgaard, M. D. Nielsen and J. Bland-Hawthorn, "Efficient multi-mode to single-mode coupling in a photonic lantern," *Optics express*, vol. 17, pp. 1988-1994, 2009.
- [3] Z. S. Eznaveh, L. J. Antonio, J. A. Zacarias, A. Schulzgen, C. Okonkwo and R. A. Correa, "All-fiber few-mode multicore photonic lantern mode multiplexer," *Optics express*, vol. 25, pp. 16701-16707, 2017.
- [4] S. Dong, H. Ding, Y. Liu and X. Qi, "Investigation of evanescent coupling between tapered fiber and a multimode slab waveguide," *Applied optics*, vol. 51, pp. 152-157, 2012.
- [5] S. G. Leon-Saval, A. Argyros and J. Bland-Hawthorn, "Photonic lanterns," *Nanophotonics*, vol. 2, pp. 429-440, 2013.
- [6] K. Li, T. Zhang, G. Liu, N. Zhang, M. Zhang and L. Wei, "Ultrasensitive optical microfiber coupler based sensors operating near the turning point of effective group index difference," *Applied Physics Letters*, vol. 109, p. 101101, 2016.
- [7] S. Lacroix, F. Gonthier and J. Bures, "Modeling of symmetric 2X2 fused fiber couplers," *Applied optics*, vol. 33.36, pp. 8361-8369, 1994.
- [8] P. Garabedian, "Free boundary flows of a viscous liquid," *Communications on Pure and Applied Mathematics*, vol. 19.4, pp. 421-434, 1966.
- [9] S. Richardson, "Two-dimensional bubbles in slow viscous flows," *Journal of Fluid Mechanics*, vol. 33.3, pp. 475-493, 1968.
- [10] S. Richardson, "Two-dimensional bubbles in slow viscous flows. Part 2," *Journal of Fluid Mechanics*, vol. 58.1, pp. 115-127, 1973.
- [11] R. W. Hopper, "Plane stokes flow driven by capillarity on free surface," *Journal of Fluid Mechanics*, vol. 213, pp. 349-375, 1990.
- [12] R. W. Hopper, "Coalescence of two viscous cylinders by capillarity: part 1, theory," *Journal of the American Ceramic Society*, vol. 76.12, pp. 2947-2952, 1993.

- [13] R. W. Hopper, "Coalescence of two viscous cylinders by capillarity: part 2, shape evolution," *Journal of the American Ceramic Society*, vol. 76.12, pp. 2953-5960, 1993.
- [14] S. Richardson, "Two-dimensional Stokes flows with time-dependent free boundaries driven by surface tension," *European Journal of Applied Mathematics*, vol. 8.4, pp. 311-329, 1997.
- [15] S. Richardson, "Plane Stokes flows with time-dependent free boundaries in which the fluid occupies a doubly-connected region," *European Journal of Applied Mathematics*, vol. 11.3, pp. 249-269, 2000.
- [16] E. Pone, X. Daxhelet and S. Lacroix, "Refractive index profile of fused-tapered fiber couplers," *Optics express*, vol. 12, pp. 2909-2918, 2004.
- [17] S. B. Pope, *Turbulent flows*, IOP Publishing, 2001.
- [18] D. A. Drew, "Mathematical modeling of two-phase flow," *Annual review of fluid mechanics*, vol. 15, pp. 261-291, 1983.
- [19] K. A. Rejniak, H. J. Kliman and L. J. Fauci, "A computational model of the mechanics of growth of the villous trophoblast bilayer," *Bulletin of mathematical biology*, vol. 66, pp. 199-232, 2004.
- [20] K. A. Rejniak, "An immersed boundary framework for modelling the growth of individual cells: an application to the early tumour development," *Journal of theoretical biology*, vol. 247, pp. 186-204, 2007.
- [21] A.-L. Dessimoz, L. Cavin, A. Renken and L. Kiwi-Minsker, "Liquid-liquid two-phase flow patterns and mass transfer characteristics in rectangular glass microreactors," *Chemical Engineering Science*, vol. 63, pp. 4035-4044, 2008.
- [22] E. Maitre, "Review of numerical methods for free interfaces," Ecole Thematique, Les Houches, 2006.
- [23] G. Tryggvason, B. Bunner, A. Esmaeeli, D. Juric, N. Al-Rawahi, W. Tauber, J. Han, S. Nas and Y. J. Jan, "A Front tracking method for the computations of multiphase flow," *Journal of computational physics*, vol. 169, pp. 708-759, 2001.
- [24] G. Tryggvason, R. Scardovelli and S. Zaleski, *Direct numerical simulations of gas-liquid multiphase flows*, Cambridge University Press, 2011.

- [25] C. S. Peskin, "The immersed boundary method," *Acta numerica*, vol. 11, pp. 479-517, 2002.
- [26] C. S. Peskin, "Numerical analysis of blood flow in the heart," *Journal of computational physics*, vol. 25.3, pp. 220-252, 1977.
- [27] A. M. Roma, C. S. Peskin and M. J. Berger, "An adaptive version of the immersed boundary method," *Journal of computational physics*, vol. 153.2, pp. 509-534, 1999.
- [28] Y. Li, A. Yun, D. Lee, J. Shin, D. Jeong and J. Kim, "Three-dimensional volume-conserving immersed boundary model for two-phase fluid flows," *computation methods application mechanical engineer*, vol. 257, pp. 36-46, 2013.
- [29] C. W. Hirt and B. D. Nichols, "Volume of fluid (VOF) method for the dynamics of free boundary," *Journal of computational physics*, vol. 39.1, pp. 201-225, 1981.
- [30] N. Balcázar, L. Jofre, O. Lehmkuhl, J. Castro and J. Rigola, "A finite-volume/level-set method for simulating two-phase flows on unstructured grids," *International journal of multiphase flow*, pp. 55-72, 2014.
- [31] D. Jacqmin, "Calculation of two-phase Navier-Stokes flows using Phase-Field modeling," *Journal of computational physics*, vol. 155, pp. 96-127, 1999.
- [32] J. Kim, "Phase field models for multi-component fluid flows," *Communications in Computational Physics*, vol. 12.3, pp. 613-661, 2012.
- [33] J. Mohd-Yusof, "Combined immersed-boundary/b-spline methods for simulations of flow in complex geometries, in: Annual Research Briefs," Center for Turbulence Research, 1997.
- [34] E. Fadlun, R. Verzicco, P. Orlandi and J. Mohd-Yusof, "Combined immersed-boundary finite-difference methods for three-dimensional complex flow simulations," *Journal of computational physics*, vol. 161, no. 1, pp. 35-60, 2000.
- [35] V. Rutka and Z. Li, "An explicit jump immersed interface method for two-phase Navier–Stokes equations with interfaces," *Computer Methods in Applied Mechanics and Engineering*, vol. 197, pp. 2317-2328, 2008.
- [36] S. Patankar, Numerical Heat Transfer and Fluid Flow, CRC press, 1980.
- [37] L. Lee and R. J. Leveque, "An immersed interface method for incompressible Navier-Stokes equations," *SIAM Journal on Scientific Computing*, vol. 25, pp. 832-856, 2003.

- [38] M. N. Linnick and H. F. Fasel, "A high-order immersed interface method for simulating unsteady incompressible flows on irregular domains," *Journal of Computational Physics*, vol. 204, pp. 157-192, 2005.
- [39] T. Kempe and F. Jochen, "An improved immersed boundary method with direct forcing for the simulation of particle laden flows," *Journal of Computational Physics*, vol. 231, pp. 3663-3684, 2012.
- [40] T. Kempe, M. Lennartz, S. Schwarz and J. Fröhlich, "Imposing the free-slip condition with a continuous forcing immersed boundary method," *Journal of Computational Physics*, vol. 282, pp. 183-209, 2015.
- [41] Y. Li, E. Jung, W. Lee, H. G. Lee and J. Kim, "Volume preserving immersed boundary methods for two-phase fluid flows," *International Journal for Numerical Methods in Fluids*, vol. 69.4, pp. 842-858, 2012.
- [42] Y. Bao, A. Donev, B. E. Griffith, D. M. McQueen and C. S. Peskin, "An Immersed Boundary method with divergence-free velocity interpolation and force spreading," *Journal of Computational Physics*, vol. 347, pp. 183-206, 2017.
- [43] R. Glowinski, P. Tsorng-Whay and J. Periaux, "Distributed Lagrange multiplier methods for incompressible viscous flow around moving rigid bodies," *Computer methods in applied mechanics and engineering*, vol. 151, pp. 181-194, 1998.
- [44] R. Glowinski, T. Pan, T. Hesla, D. Joseph and J. Periaux, "A fictitious domain approach to the direct numerical simulation of incompressible viscous flow past moving rigid bodies: application to particulate flow," *Journal of Computational Physics*, vol. 169, pp. 363-426, 2001.
- [45] Z. Yu, N. Phan-Thien, Y. Fan and R. I. Tanner, "Viscoelastic mobility problem of a system of particles," *Journal of non-newtonian fluid mechanics*, vol. 104, pp. 87-124, 2002.
- [46] Z. Yu, N. Phan-Thien and R. Tanner, "Dynamic simulation of sphere motion in a vertical tube," *Journal of Fluid Mechanics*, vol. 518, pp. 61-93, 2004.
- [47] Z. Yu, "A DLM/FD method for fluid/flexible-body interactions," *Journal of computational physics*, vol. 207, pp. 1-27, 2005.
- [48] K. Taira and T. Colonius, "The immersed boundary method: a projection approach," *Journal of Computational Physics*, vol. 225, pp. 2118-2137, 2007.

- [49] Y. Feldman and Y. Gulberg, "An extension of the immersed boundary method based on the distributed Lagrange multiplier approach," *Journal of Computational Physics*, vol. 322, pp. 248-266, 2016.
- [50] Y. Feldman and A. Y. Gelfgat, "On pressure-velocity coupled time-integration of incompressible Navier-Stokes equations using direct inversion of Stokes operator or accelerated multigrid technique," *Computers & Structures*, vol. 87, no. 11, pp. 710-720, 2009.
- [51] Y. Feldman and Y. Gulberg, "An extension of the immersed boundary method based on the distributed Lagrange multiplier approach," *Journal of Computational Physics*, vol. 322, pp. 248-266, 2016.
- [52] A. Spizzichino, S. Goldring and Y. Feldman, "The immersed boundary method: application to two-phase immiscible flows," *Commun. Comput. Phys*, vol. 25, pp. 107-134, 2019.
- [53] Y. Feldman, "Semi-implicit direct forcing immersed boundary method for incompressible viscous thermal flow problems: A Schur complement approach," *International Journal of Heat and Mass Transfer*, vol. 127, pp. 1267-1283, 2018.
- [54] M. Uhlmann, "An immersed boundary method with direct forcing for the simulation of particulate flows," *Journal of Computational Physics*, vol. 209, pp. 448-476, 2005.
- [55] R. H. Pletcher, J. C. Tannehill and D. Anderson, *Computational Fluid mechanics and heat transfer*, CRC Press, 1997.
- [56] S. Hysing, S. Turek, D. Kuzmin, N. Parolini, E. Burman, S. Ganesan and L. Tobiska, "Quantitative benchmark computations of two-dimensional bubble dynamics," *International Journal for Numerical Methods in Fluids*, vol. 60.11, pp. 1259-1288, 2009.
- [57] G. Tryggvason, R. Scardovelli and S. Zaleski, *Direct numerical simulations of gas-liquid multiphase flows*, Cambridge University Press, 2011.
- [58] F. H. Harlow and J. E. Welch, "Numerical calculation of time-dependent viscous incompressible flow of fluid with free surface," *The physics of fluids*, vol. 8.12, pp. 2182-218, 1965.
- [59] P. R. Amestoy, I. S. Duff, J.-Y. L'Excellent and J. Koster, "A fully asynchronous multifrontal solver using distributed dynamic scheduling," *SIAM Journal on Matrix Analysis and Applications*, vol. 23.1, pp. 15-41, 2001.

- [60] P. R. Amestoy, A. Buttari, J.-Y. L'Excellent and T. Mary, "Performance and scalability of the block low-rank multifrontal factorization on multicore architectures," *ACM Transactions on Mathematical Software (TOMS)*, vol. 45, pp. 1-36, 2019.
- [61] J. Klostermann, K. Schaake and R. Schwarze, "Numerical simulation of a single rising bubble by VOF with surface compression," *International Journal for Numerical Methods in Fluids*, vol. 71.8, pp. 960-982, 2013.
- [62] T. Chinyoka, Y. Renardy, M. Renardy and D. Khismatullin, "Two-dimensional study of drop deformation under simple shear for Oldroyd-B liquids," *Journal of Non-Newtonian Fluid Mechanics*, vol. 130, pp. 45-56, 2005.
- [63] K. S. Sheth and C. Pozrikidis, "Effect of inertia on the deformation of liquid drops in simple shear flow," *Computers & Fluids*, vol. 24.2, pp. 101-119, 1995.
- [64] F. Ilinca and J.-F. Hétu, "Immersed Boundary Solution of Natural Convection in a Square Cavity with an Enclosed Rosette-Shaped Hot Cylinder," *Numerical Heat Transfer, Part A: Applications*, vol. 65.12, pp. 1154-1175, 2014.
- [65] D. Gaudlitz and N. A. Adams, "On improving mass-conservation properties of the hybrid particle-level-set method," *Computers and Fluids*, vol. 37, pp. 1320-1331, 2008.
- [66] Z. Wang, J. Yang and F. Stern, "An improved particle correction procedure for the particle level set method," *Journal of Computational Physics*, vol. 228, pp. 5819-5837, 2009.
- [67] P. J. Archer and W. Bai, "A new non-overlapping concept to improve the Hybrid Particle Level Set method in multi-phase fluid flows," *Journal of Computational Physics*, vol. 282, pp. 317-333, 2015.
- [68] R. Clift, J. R. Grace and M. E. Weber, *Bubbles, Drops, and Particles*, New York: Academic press, 1978.
- [69] S.-R. Hysing, "Numerical simulation of immersed fluids with FEM level set techniques," Techn. Univ, 2007.
- [70] M. Kronbichler and G. Kreiss, "A hybrid level-set-phase-field method for two-phase flow with contact lines," University of Uppsala, 2011.

- [71] H. Wadell, "Sphericity and roundness of rock particles," *The Journal of Geology*, vol. 41, no. 3, pp. 310-331, 1933.
- [72] T. Fu, Y. Ma and H. Z. Li, "Hydrodynamic feedback on bubble breakup at a T-junction within an asymmetric loop," *AIChE Journal*, vol. 60, no. 5, pp. 1920-1929, 2014.
- [73] Y. Song, P. Manneville and C. N. Baroud, "Local interactions and the global organization of a two-phase flow in a branching tree," *Physical review letters*, vol. 105, no. 13, p. 134501, 2010.
- [74] A. Leshansky and L. Pismen, "Breakup of drops in a microfluidic T junction," *Physics of Fluids*, vol. 21, no. 2, p. 023303, 2009.
- [75] J. Li, Y. Y. Renardy and M. Renardy, "Numerical simulation of breakup of a viscous drop in simple shear flow through a volume-of-fluid method," *Physics of Fluids*, vol. 12, no. 2, pp. 269-282, 2000.
- [76] T. A. Birks and Y. W. Li, "The shape of fiber tapers," *Journal of Lightwave Technology*, vol. 10.4, pp. 432-438, 1992.
- [77] A. D. Yablon, *Optical fiber fusion splicing*, vol. 103, Springer Science and Business Media, 2005.
- [78] N. P. Bansal and R. H. Doremus, *Handbook of glass properties*, Elsevier, 2013.
- [79] Y. Kikuchi, H. Sudo and N. Kuzuu, "OH content dependence of viscosity of Vitreous Silica," *Journal of the Ceramic Society of Japan*, vol. 105, pp. 645-649, 1997.
- [80] Y. Shamir, Y. Sintov and M. Shtaif, "Beam quality analysis and optimization in an adiabatic low mode tapered fiber beam combiner," *Optical Society of America*, vol. 27, pp. 2669-2676, 2010.
- [81] T. L. Bergman, F. P. Incropera, D. P. DeWitt and A. S. Lavine, *Fundamentals of heat and mass transfer*, John Wiley and Sons, 2011.
- [82] A. Spizzichino, S. Goldring and Y. Feldman, "Prediction of the Structure and Refractive Index Profile of Fused Fiber Optic Components: A Numerical and Experimental Study," *Physical Review E*, *under review*.

Appendix I

Heat transfer problems that involve surface convection effects are governed by the Biot number, which provides a measure of the temperature drop in the solid relative to the temperature difference between the solid surface and the fluid. The Biot number may be interpreted as a ratio of thermal resistances:

$$Bi = \frac{hL}{k_{fs}}, \quad (7.1)$$

where k_{fs} , h , and L are the thermal conductivity, convection heat transfer coefficient, and characteristic length, respectively. In particular, if $Bi \ll 1$, the assumption of a uniform temperature distribution within the solid is reasonable [81]. For the case of optical fibers (fused silica), the fibers are the cylinders interacting with the surrounding air. The characteristic length of a typical fiber is $L = \frac{V_{fiber}}{A_s} = \frac{D}{4}$, while the convection coefficient h for the natural convection heat transfer between the horizontal cylinder and the surrounding air can be assessed by [81]:

$$h = \frac{k}{D} \left\{ 0.6 + \frac{0.387 Ra_D^{1/6}}{\left[1 + (0.559 / Pr)^{9/16} \right]^{8/27}} \right\}^2, \quad (7.2)$$

Where the Prandtl (Pr) and Rayleigh (Ra_D) numbers are:

$$Pr = \frac{\mu C}{k}, \quad (7.3)$$

where μ - fluid viscosity, C - fluid specific heat, and k - fluid thermal conductivity.

$$Ra_D = Gr \cdot Pr, \quad (7.4)$$

$$Gr_D = D^3 \rho^2 g \Delta T \beta / \mu^2, \quad (7.5)$$

where ρ - fluid density, g - gravitational acceleration, and β - fluid thermal expansion coefficient. Substitution of characteristic length $D = 31.25 \mu m$, $g = 9.81 m / s^2$, and $\Delta T = 1900 K$ with the values of dynamic properties of air given in Table 13 in Eq. (7.2) yields $h = 357 \frac{W}{m^2 \cdot K}$.

Table 13- The values of dynamic properties of air.

| μ | C | k | ρ | β | Pr | Gr | Ra |
|------------|------------|-----------|------------|---------|------|---------|---------|
| $kg / m s$ | $J / kg K$ | $W / m K$ | kg / m^3 | $1 / K$ | | | |
| 58E-6 | 1.25E3 | 106E-3 | 0.1885 | 3400E-6 | 0.68 | 2.07E-5 | 1.41E-5 |

The thermal conductivity of fused silica is $k_{fs} = 1.4 \frac{W}{m \cdot K}$. Substitution into Eq. (7.1) yields $Bi = \frac{358 \cdot 31.25E-6}{1.4} \approx 0.008$, which justifies the assumption of uniform temperature of the fibers during the process.

Moreover, comparison of the heat transfer by conduction, by convection and by radiation indicate that heat flux by convection is $q'' = h \Delta T = 6.6E5 W / m^2$ while the heat flux by radiation is $q'' = \sigma(T_a^4 - T_b^4) = 7E5 W / m^2$. Thus, both heat transfer mechanisms are of the same order of magnitude and can be safely neglected compared to the conduction heat transfer.

Appendix II

The error bars shown in the graphs in chapter 6 reflect uncertainties of the experimental measurements. The horizontal error bars attached to the fusion time measurements express uncertainty of the specific location of the cross-section along the coupler axis. We estimate the uncertainty of the slicer (the micrometer screw with the polish paper) to be bounded by $\Delta = \pm 100 \mu m$. This value is related to the corresponding time interval estimated by $\Delta t = \Delta / 2v_s = \pm 66 s$.

The vertical error bars correspond to uncertainties inherent to measurements of the cross-section characteristic length and area. Prior to recording the cross-section of each coupler, a fiber picture with an a priori known reference diameter was taken, in order to calculate the number of pixels per 100 micrometers. Thus, the estimated uncertainty of the calculated ratio is $\Delta = \pm 3Px$, due to the boundary thickness of the fiber. The measurements of H and W (see Eq. (5.2)) were sampled with the same error. The error bars in the graphs in chapter 6 correspond to maximum and minimum values yielded by combinations of these values.

תקציר

מצמדים ורכיבים מבוססי סיבים אופטיים נמצאים בשימוש נרחב במערכות אופטיות. רכיבים אלו מאפשרים לצמד אור בין שני סיבים (מצמד דו סיבי), או לאגד ולפצל אור ממספר סיבים לתוך סיב אחד מרכזי (מחבר סיבי). המשותף לכל רכיבים אלו הוא תהליך הייצור הכולל חימום, משיכה והיתוך (הצמדה) של הסיבים המשיקים זה לזה עד לכדי קבלת הרכיב האופטי. תפקודו האופטי של המצמד נקבע על ידי המבנה הגיאומטרי החיצוני ופרופיל מקדם השבירה הפנימי המוגדר על ידי פילוג ריכוז מאלחים בתוך הסיבים. קיימות שיטות חישוביות ותוכנות רבות המאפשרות לחזות את ההתנהגות האופטית של המצמד בהינתן צורתו החיצונית ופרופיל מקדם השבירה. מחקרים קודמים הציעו מודלים לחיזוי מבנה הסיב. יחד עם זאת, הכלים הקיימים אינם מספקים דיוק מספק, ולכך תוצאות סימולציות לחיזוי ההתנהגות האופטית מכל סוג לא תהיה מדויקת ללא הקלט הנכון. בהיעדר יכולת סימולציה מתאימה, פיתוחם של רכיבים ומצמדים אופטיים מצריכים נסיונות חוזרים בשיטת ניסוי וטעיה, שהופכים את תהליך הפיתוח לארוך ויקר. מטרת מחקר זה היא לתת מענה גנרי, מבוסס חישובים נומריים לחיזוי התפתחות ושינוי המבנה של רכיבי סיבים אופטיים הכוללים מספר רב של סיבים ובכל תצורה. בנוסף, הכלי הנומרי יכלול מרכיב לפתרון משוואת ההסעה-דיפוזיה (convection-diffusion) המגדירים את ריכוזי המאלחים בתוך הסיבים בתהליך הייצור. בנוסף, הפותרן הנומרי פותח כך שיתאפשר לבצע בו שימוש אפליקטיבי לפתרון בעיות שונות המשלבות זרימה דו פאזית מתחומים פיזיקליים שונים. המחקר בוצע בשני שלבים: א- פותחה התשתית הנומרית והכלי לביצוע הסימולציות, ב- בוצעו ניסויים ואפיון ההתפתחות הדינמית של רכיבים אופטיים במהלך ייצורם. ובוצעה השוואה בין תוצאות הניסויים לתוצאות הסימולציות הנומריות לחיזוי מבנה הרכיבים.

תחילה, פותחה גישה חדשנית המבוססת על שיטת Immersed Boundary בשילוב עם Front Tracking method. גישה זו מאפשרת לפתור את משוואות שימור מסה ושימור תנע עבור זרימה דו פאזית בלתי דחיסה באופן מצומד כך שהלחץ ומתח הפנים בין הפאזות משמשים ככופלי לאגרנג'. אחד היתרונות הבולטים של שימוש זה הוא קיום משוואת שימור מסה (עם או ללא מקור) implicit, ומניעת זליגה של חומר מהגוף הנע.

הגישה הנומרית שפותחה יושמה לכדי פותרן דו מימדי ממשי ונבחנה באופן מעמיק על ידי השוואה לארבעה בעיות ידועות הנבדלות זו מזו בכח המניע של התנועה. בעיות הבוחן שנבחנו כללו גוף העולה ומשנה את צורתו כתוצאה מכוחות ציפה, גוף הנמצא תחת השפעת גזירה, גוף בצורת

רוזטה שמשנה את צורתו לעיגול כתוצאה מכוחות מתח הפנים. בנוסף, נבחנו גם בעיות שכללו פיצול של הגוף בעקבות יחס צפיפויות ושדה מהירויות גבוה. פתרונות והשוואת כל בעיות הבורח לתוצאות הידועות בספרות העידו על התאמה טובה ופתרון נכון ומדויק של הבעיה. חלק זה של המחקר פורסם ב 2019 בכתב העת "Communication of Computational Physics".

לאחר הנחת היסודות הנומריים, החל השלב השני ובו בוצעו ניסויים לייצור ומיפוי מצמדים אופטיים, ביצוע סימולציות ובחינת תוצאות הסימולציה אל מול תוצאות הניסויים. ההשוואה בוצעה עבור ארבעה מצמדים מסוגים שונים: הראשון סימטרי לחלוטין ומורכב משני סיבי SMF. השני מורכב משני סיבים בעלי קוטר חיצוני זהה, אך לאחד הסיבים קוטר הליבה גדול (האיזור בו ריכוז המאלחים גבוהה). המצמד השלישי אינו סימטרי כלל, כלומר שני הסיבים בקוטר חיצוני ופרופיל מקדם שבירה שונה. הקונפיגורציה הרביעית היא בעלת המבנה המסובך ביותר, וכללה דיקוק לסיב בעל חתך לא אופייני (לא עגול). עבור כל המקרים התקבלו התאמות טובות, בהשוואה איכותית וכמותית בין תוצאות הניסוי לסימולציה הנומרית. בכל המקרים, שדה המהירויות התקבל על-ידי פתרון משוואות הרציפות ומשוואות המומנטום (continuity and Navier-Stokes), והשינוי בריכוז המאלחים התקבל על ידי פתרון משוואה הסעה-דיפוזיה. בנוסף, בוצעה התייחסות לירידה בצמיגות הסיבים כתוצאה מבליעת OH במהלך ייצור המצמדים. חלק זה של המחקר הניב מאמר נוסף, שהתקבל לכתב העת Physical Review E.

פרט להשוואה בין תוצאות הסימולציות הנומריות לניסויים, בוצעו סימולציות נוספות לאפיון מצמדים בקונפיגורציות לא סימטריות ביחסים שונים על מנת לאפיין את הקשר בין יחס אורך-רוחב של המצמד, לבין מידת ההיתוך של המצמד.

בנוסף, הכלי הנומרי מסוגל לתת המענה לסימולציות של מבנים מורכבים הכוללים מספר רב של סיבים ונקודות מגע בניהם, הכוללים אויר כלוא בין הסיבים. דוגמה לסימולציה נומרית למבנה מורכב הכולל שבעה סיבים עם מספר נקודות מגע לכל סיב ואזורים בהם נכלא אויר בניהם, מוצגת בעבודה.

מילות מפתח:

ייצור רכיבי סיבים אופטיים, איחוי סיבים, סימולציות נומריות, זרימה דו-פאזית, שיטת גוף טבול (Immersed Boundary method).

אוניברסיטת בן גוריון בנגב

חיזוי המבנים ומקדם פרופיל השבירה
של רכיבים מבוססי סיבים אופטיים
על בסיס חישובים נומריים וניסויים

מחקר לשם מילוי חלקי של הדרישות לקבלת תואר
"דוקטור לפילוסופיה"

מאת

אביחי ספיצקי

הוגש לסינאט אוניברסיטת בן גוריון בנגב

אישור המנחה: _____

אישור דיקן בית הספר ללימודי מחקר מתקדמים ע"ש קרייטמן _____

אוקטובר 2020

תשרי תשפ"א

באר-שבע

העבודה נעשתה בהדרכת
ד"ר יורי פלדמן וד"ר שרון גולדרינג
במחלקה להנדסת מכונות
בפקולטה להנדסה

אוניברסיטת בן גוריון בנגב

חיזוי המבנים ומקדם פרופיל השבירה
של רכיבים מבוססי סיבים אופטיים
על בסיס חישובים נומריים וניסויים

מחקר לשם מילוי חלקי של הדרישות לקבלת תואר
"דוקטור לפילוסופיה"

מאת

אביחי ספיצקי

הוגש לסינאט אוניברסיטת בן גוריון בנגב

אוקטובר 2020

תשרי תשפ"א

באר-שבע